J. Fluid Mech. (2012), *vol.* 706, *pp.* 5–33.
doi:10.1017/jfm.2012.207

Boundary layer structure in turbulent Rayleigh–Bénard convection

Nan Shi‡, Mohammad S. Emran†‡ and Jörg Schumacher

Institut für Thermo- und Fluiddynamik, Technische Universität Ilmenau,
Postfach 100565, D-98684 Ilmenau, Germany

(Received 24 October 2011; revised 17 April 2012; accepted 25 April 2012;
first published online 13 June 2012)

The structure of the boundary layers in turbulent Rayleigh–Bénard convection is studied by means of three-dimensional direct numerical simulations. We consider convection in a cylindrical cell at aspect ratio one for Rayleigh numbers of $Ra = 3\times10^9$ and 3×10^{10} at fixed Prandtl number $Pr = 0.7$. Similar to the experimental results in the same setup and for the same Prandtl number, the structure of the laminar boundary layers of the velocity and temperature fields is found to deviate from the prediction of Prandtl–Blasius–Pohlhausen theory. Deviations decrease when a dynamical rescaling of the data with an instantaneously defined boundary layer thickness is performed and the analysis plane is aligned with the instantaneous direction of the large-scale circulation in the closed cell. Our numerical results demonstrate that important assumptions of existing classical laminar boundary layer theories for forced and natural convection are violated, such as the strict two-dimensionality of the dynamics or the steadiness of the fluid motion. The boundary layer dynamics consists of two essential local dynamical building blocks, a plume detachment and a post-plume phase. The former is associated with larger variations of the instantaneous thickness of velocity and temperature boundary layer and a fully three-dimensional local flow. The post-plume dynamics is connected with the large-scale circulation in the cell that penetrates the boundary region from above. The mean turbulence profiles taken in localized sections of the boundary layer for each dynamical phase are also compared with solutions of perturbation expansions of the boundary layer equations of forced or natural convection towards mixed convection. Our analysis of both boundary layers shows that the near-wall dynamics combines elements of forced Blasius-type and natural convection.

Key words: boundary layer structure, Bénard convection, turbulent convection

1. Introduction

Turbulent Rayleigh–Bénard convection can be initiated in a fluid which is confined between a cold isothermal plate at the top and a hot isothermal plate at the bottom, provided that a sufficiently strong temperature difference is sustained. In the turbulent regime, the majority of the heat is carried by convective transport through the layer or cell. It is only in the vicinity of the top and bottom plates, where the fluid

† Email address for correspondence: mohammad.emran@tu-ilmenau.de
‡ The first two authors contributed equally to this work.

velocities are small, that conductive transport takes over and becomes important. As in all other wall-bounded flows, boundary layers form. In the present system these are boundary layers of the velocity and temperature fields. The structure of these boundary layers turns out to be crucial for a deeper understanding of the local and global transport processes, as discussed for example in a recent review (Ahlers, Grossmann & Lohse 2009*b*). Furthermore, the boundary layers interact with a so-called large-scale circulation (LSC) that is always established in a closed turbulent convection cell. This LSC can take the form of a single roll for aspect ratios of order unity or multiple roll patterns for larger ones (du Puits, Resagk & Thess 2007*b*; van Reeuwijk, Jonker & Hanjalić 2008*a*; Bailon-Cuba, Emran & Schumacher 2010; Mishra *et al.* 2011). On the one hand, the LSC is triggered by packets of thermal plumes: fragments of the thermal boundary layers which detach randomly from the top and bottom plates into the bulk of the cell. On the other hand, the fully established LSC with its complex three-dimensional dynamics can be expected to affect and partly even drive the laminar flow dynamics close to the walls. This interplay has not yet been studied in detail for cylindrical convection cells and provides one central motivation for the present work.

From a global perspective the heat transport in a turbulent convection cell, which is measured by the dimensionless Nusselt number Nu, is a function of the three dimensionless control parameters in Rayleigh–Bénard convection, namely the Rayleigh number Ra, the Prandtl number Pr and the aspect ratio Γ of the convection cell, i.e. $Nu = f(Ra, Pr, \Gamma)$. Two scaling theories yield different predictions for the turbulent heat transport in convection based on different assumptions on the boundary layer structure. While the scaling theory of Shraiman and Siggia (Siggia 1994) is based on a turbulent boundary layer with a logarithmic profile for the mean streamwise velocity, Grossmann & Lohse (2000) assume laminar boundary layers of Prandtl–Blasius–Pohlhausen type (Prandtl 1905; Blasius 1908; Pohlhausen 1921) in order to estimate the boundary layer contributions to the thermal and kinetic energy dissipation rates. Such a laminar boundary layer evolves in purely *forced convection*, i.e. for a laminar flow over a flat plate. The temperature is treated as a passive scalar (Pohlhausen 1921).

Measuring the boundary layer structure is, however, difficult in laboratory experiments for high-Rayleigh-number convection. The reason is that the thickness of the thermal boundary layer, δ_T, decreases as the Rayleigh and thus the Nusselt number grow. This thickness is given by

$$\delta_T = \frac{H}{2Nu}, \tag{1.1}$$

where H is the height of the convection cell. For a convection flow at $Pr \sim O(1)$, the corresponding velocity boundary layer will have a similar thickness of $\delta_v \sim \delta_T$ and will thus decrease similarly with increasing Rayleigh number (see e.g. Shishkina *et al.* 2010). Detailed measurements of boundary layer profiles at higher Rayleigh numbers ($Ra > 10^9$) thus require large devices such as the 'Barrel of Ilmenau' for the convection in air (du Puits, Resagk & Thess 2007*a*, 2010) or high-resolution particle image velocimetry, as is possible for convection in water (Sun, Cheung & Xia 2008; Zhou & Xia 2010*a*). Statistical time series analyses of the mean temperature and velocity profiles in the boundary layer yielded deviations from the predicted laminar Blasius profiles (du Puits *et al.* 2007*a*; Zhou & Xia 2010*a*). A dynamic rescaling of the data with respect to an instantaneous boundary layer thickness (which will be explained further below in the text) tends to bring it closer to the Blasius prediction in the water experiment by Zhou & Xia (2010*a*). The latter result was also confirmed by

a series of two-dimensional direct numerical simulations by Zhou *et al.* (2010, 2011). However, in both cases, the large-scale circulation is a (quasi-) two-dimensional flow which cannot fluctuate in the third direction.

Du Puits *et al.* (2007*a*) concluded from their work that the deviations from the Blasius shape arise due to the characteristic near-wall coherent structures – so-called thermal plumes – which permanently detach from the thermal boundary layer. Direct numerical simulation (DNS) by van Reeuwijk, Jonker & Hanjalić (2008*b*) for Rayleigh numbers up to 10^8 supports systematic deviations from a laminar boundary layer on the basis of an analysis of the friction factor and the Reynolds stress budgets. Their DNS showed that the integral of the streamwise pressure gradients have a large magnitude compared to Reynolds stresses and are not zero as in the Blasius case. Recall also that the active nature of the temperature field is not incorporated in Prandtl–Blasius–Pohlhausen theory.

Similarity solutions for *natural convection*, complementary to Prandtl–Blasius–Pohlhausen theory for forced convection, are well known (see e.g. Stewartson 1958; Rotem & Claassen 1969). Here the buoyancy term remains in the momentum equation (see below) and is balanced by a wall-normal pressure gradient. The temperature differences now initiate fluid motion. Both purely forced and natural convection were subject to perturbation expansions towards *mixed convection*, which combines forced and natural convection (Sparrow & Minkowycz 1962). This means that either the active role of temperature is included as a small-size effect in forced convection or a weak outer flow is imposed in natural convection. Hieber (1973) solved numerically the equations which arise from perturbative expansions of forced and natural convection. These classical studies are combined with more recent efforts to develop two-dimensional boundary layer models for the plume detachment (Fuji 1963; Theerthan & Arakeri 1998; Puthenveettil & Arakeri 2005; Puthenveettil *et al.* 2011). The models assume two-dimensional line-like thermal plumes with no significant variation perpendicular to the flow plane.

In this work, we want to resolve the boundary layer structure and its relation to the large-scale circulation for $Ra > 10^9$ by means of three-dimensional DNS. We aim at better understanding of the physical reasons for the deviations of the boundary layer profiles from the classical Prandtl–Blasius–Pohlhausen and Stewartson theories for forced and natural convection, respectively. We therefore conduct two long-time direct numerical simulations of turbulent Rayleigh–Bénard convection in a cylindrical cell at an aspect ratio $\Gamma = 1$. Step by step we test which assumptions of the original derivations of the similarity solutions are satisfied. Our studies will include analyses of the LSC, the pressure gradient fluctuations, the importance of violations of the two-dimensionality of the flow and the active role of the temperature at the isothermal walls. The coupling between the two boundary layers is also analysed. We will show that in fact most of the original assumptions of all boundary layer theories are not established in the present cellular flow. Furthermore, we relate locally measured turbulence profiles with the results from idealized mixed convection boundary layers.

The outline of the paper is as follows. In the next section, we summarize the numerical model and the equations of motion. We then present the boundary layer profiles from the classical time series analysis and the dynamical rescaling procedure. The studies are followed by investigations of the large-scale circulation, the pressure fluctuations, and time variations of the local boundary layer structure. In § 4 we resolve the dynamics in the boundary layer in a small observation window and relate

the findings to results of the boundary layer theory of mixed convection. We conclude our work with a summary and an outlook.

2. Numerical model

The three-dimensional Navier–Stokes equations in the Boussinesq approximation are solved in combination with an advection–diffusion equation for the temperature field. The system of equations is given by

$$\frac{\partial u_i}{\partial t} + u_j \frac{\partial u_i}{\partial x_j} = -\frac{\partial p}{\partial x_i} + \nu \frac{\partial^2 u_i}{\partial x_j^2} + \alpha g T \delta_{iz}, \tag{2.1}$$

$$\frac{\partial u_i}{\partial x_i} = 0, \tag{2.2}$$

$$\frac{\partial T}{\partial t} + u_j \frac{\partial T}{\partial x_j} = \kappa \frac{\partial^2 T}{\partial x_j^2}, \tag{2.3}$$

where $i, j = x, y, z$. Here $p(x, y, z, t)$ is the kinematic pressure, $u_i(x, y, z, t)$ the velocity field, $T(x, y, z, t)$ the total temperature field, ν the kinematic viscosity, and κ the diffusivity of the temperature. The dimensionless control parameters, the Rayleigh number Ra, the Prandtl number Pr, and the aspect ratio Γ are defined by

$$Ra = \frac{g\alpha \Delta T H^3}{\nu\kappa}, \quad Pr = \frac{\nu}{\kappa}, \quad \Gamma = \frac{2R}{H}. \tag{2.4}$$

Our studies are conducted for $\Gamma = 1$, $Pr = 0.7$ and $Ra = 3 \times 10^9$ and 3×10^{10}. Constant α is the thermal expansion coefficient, g the gravitational acceleration, ΔT the outer temperature difference, R the radius and H the height of the cylindrical cell. The characteristic length is H, the characteristic velocity is the free-fall velocity $U_f = \sqrt{g\alpha \Delta T H}$. Times are consequently given in units of the free-fall time $T_f = H/U_f$. The cylindrical geometry requires a switch from Cartesian to cylindrical coordinates, $(x, y, z) \to (r, \phi, z)$. No-slip boundary conditions for the velocity field components, i.e. $u_i \equiv 0$, hold at all walls. The top and bottom plates are held isothermal at fixed temperatures T_{bottom} and T_{top}, respectively. The sidewalls are adiabatic with $\partial T/\partial r = 0$. The grid resolutions are $N_r \times N_\phi \times N_z = 301 \times 513 \times 360$ for $Ra = 3 \times 10^9$ and $513 \times 1153 \times 861$ for $Ra = 3 \times 10^{10}$, where N_r, N_ϕ and N_z are the number of grid points in the radial, azimuthal and axial directions respectively.

The equations are discretized on a staggered grid with a second-order finite difference scheme (Verzicco & Orlandi 1996; Verzicco & Camussi 2003). The pressure field p is determined by a two-dimensional Poisson solver after applying a one-dimensional fast Fourier transform (FFT) in the azimuthal direction. The time advancement is done by a third-order Runge–Kutta scheme. The grid spacings are non-equidistant in the radial and vertical directions. In the vertical direction, the grid spacing is close to Chebyshev collocation points. The grid resolutions are chosen such that the criterion by Grötzbach (1983) is satisfied plane by plane. We therefore define a height-dependent Kolmogorov scale as

$$\eta_K(z) = \frac{\nu^{3/4}}{\langle \epsilon\,(z) \rangle_{A,t}^{1/4}}, \tag{2.5}$$

where the symbol $\langle \cdot \rangle_{A,t}$ denotes an average over a plane at a fixed height z and an ensemble of statistically independent snapshots. Following Emran & Schumacher

(2008) and Bailon-Cuba *et al.* (2010), we define the maximum of the geometric mean of the grid spacing at height z by $\tilde{\Delta}(z) = \max[\sqrt[3]{r\Delta_\phi \Delta_r(r)\Delta_z(z)}]$. The thermal boundary layer is resolved with 18 grid planes for $Ra = 3 \times 10^9$ and with 23 grid planes for $Ra = 3 \times 10^{10}$. Thus the recently discussed resolution criterion (Shishkina *et al.* 2010), which would result in 9 and 13 grid planes for the thermal boundary layer, is satisfied and over-resolved by almost a factor of 2 in both cases.

The Nusselt number is found to be $Nu = 90.32 \pm 0.63$ for $Ra = 3 \times 10^9$ with a standard deviation of 0.7 %. The second run at $Ra = 3 \times 10^{10}$ resulted in $Nu = 189.65 \pm 1.5$, which gives a standard deviation of 0.8 %. The standard deviation is determined in the same way as in Bailon-Cuba *et al.* (2010). We take the Nusselt number plane by plane and determine the fluctuation about the global mean.

Figure 1 displays instantaneous three-dimensional velocity fields viewed from the top to the edge of the boundary layer close to the bottom plate for two Rayleigh numbers. Although a preferential mean flow direction is observable, we see significant deviations from two-dimensionality as visible by the wavy streamlines. With increasing Rayleigh number the streamline plot shows more and more textures on an ever finer scale.

3. Boundary layer analysis

3.1. *Vertical mean profiles from time series analysis*

Our numerical approach follows the experimental procedure. The latter consists of measuring time series of the three velocity components or temperature at a given point (r, ϕ, z) in the cell, computing time-averages and repeating the measurement for different values of z. The results of such procedures are mean profiles of temperature or velocity. In our direct numerical simulation we compute such time series simultaneously for an array of 40 (and 100) points starting from $z = H$. Probe array 1 is at the centreline. Probe arrays 2, 3 and 4 are at $r = 0.88R$ and $\phi = 0, \pi/2$ and π, respectively (see figure 2*a*). We compare the one-dimensional mean profiles for the horizontal velocity V (as defined in du Puits *et al.* 2007*a*), which is given by

$$V(r, \phi, z, t) = \sqrt{u_r^2(r, \phi, z, t) + u_\phi^2(r, \phi, z, t)}, \tag{3.1}$$

the vertical velocity component u_z and the normalized temperatures Ξ from the top (t) and bottom (b) plates, which are defined by

$$\Xi^t(r, \phi, z, t) = \frac{T(z = H/2) - T(r, \phi, z, t)}{T(z = H/2) - T_{top}}, \tag{3.2}$$

$$\Xi^b(r, \phi, z, t) = \frac{T(r, \phi, z, t) - T(z = H/2)}{T_{bottom} - T(z = H/2)}, \tag{3.3}$$

with the corresponding profiles arising from Prandtl–Blasius–Pohlhausen theory (see figure 2*b–d*). Here η is the similarity variable defined in the Appendix in (A 1). The time series contains 57 000 data points for $Ra = 3 \times 10^9$ (and 23 000 for $Ra = 3 \times 10^{10}$) at each position of the probe array. This corresponds to 122 (and 58 for $Ra = 3 \times 10^{10}$) free-fall time units T_f. Similar to the laboratory experiments by du Puits *et al.* (2007*a*) and Zhou & Xia (2010*a*), we detect clear deviations from the Blasius and Pohlhausen solutions, which are also shown in the figures. Furthermore, significant differences can be seen between the four profiles, which are caused by the existing large-scale flow in the cell. Our profiles at $Ra = 3 \times 10^9$ suggest that probe array 4 (and probably array 3 as well) are significantly altered by a mean downward motion, while probe

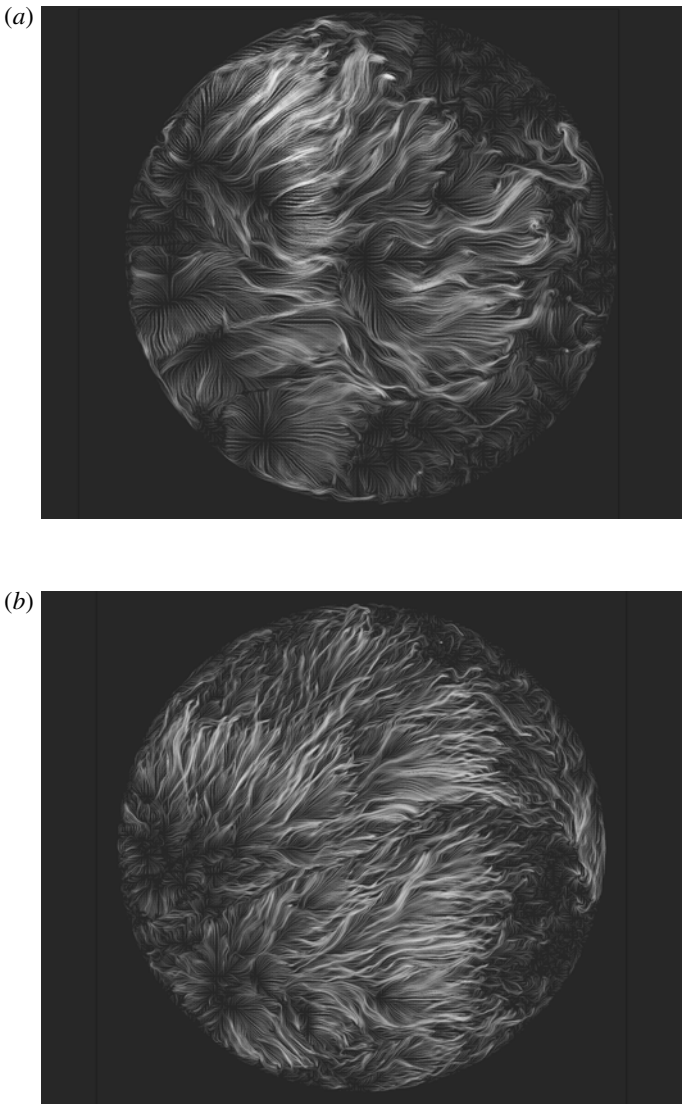

FIGURE 1. Snapshot of three-dimensional streamlines in a turbulent convection cell viewed from the top of the boundary layer plane. The lines are seeded in a horizontal plane inside the thermal boundary layer. (*a*) $Ra = 3 \times 10^9$, (*b*) $Ra = 3 \times 10^{10}$.

array 2 is the region of mean upward motion. The mean downward motion seems to be connected with an increase of the boundary layer thickness as the data relax much more slowly to the Blasius profile. In § 3.4 we will show that the LSC is on average almost perfectly aligned with the x-axis ($\phi = 0$) for the time interval considered in this particular run. In figure 3, we compare the data for the two Rayleigh numbers at the centreline. The differences between the two data sets are very small.

3.2. *Dynamical rescaling and fluctuations of the boundary layer thickness*

In the next step, we follow the idea of Zhou & Xia (2010*a*), which was applied in their convection experiment in a narrow rectangular cell, and investigate whether

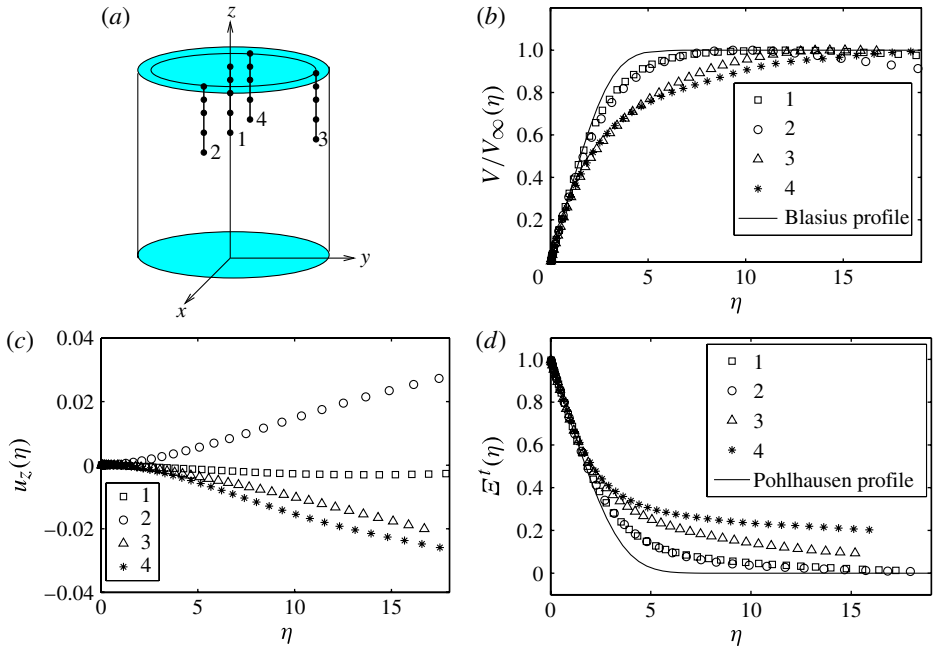

FIGURE 2. (Colour online available at journals.cambridge.org/flm) Mean profiles of velocity and temperature at $Ra = 3 \times 10^9$. (*a*) Sketch of the four probe arrays with measurement locations. Probe array 1 is mounted at $(r, \phi) = (0, 0)$, array 2 at $(0.88R, 0)$, array 3 at $(0.88R, \pi/2)$ and array 4 at $(0.88R, \pi)$. (*b*) Mean profile of the horizontal velocity $V(\eta)$ as defined in (3.1). (*c*) Mean profile of the vertical velocity component $u_z(\eta)$. (*d*) Mean profile of the rescaled temperature $\Xi^t(\eta)$ which is given by (3.3). The solid lines in (*b*) and (*d*) correspond to the classical Blasius and Pohlhausen solutions (Schlichting 1957).

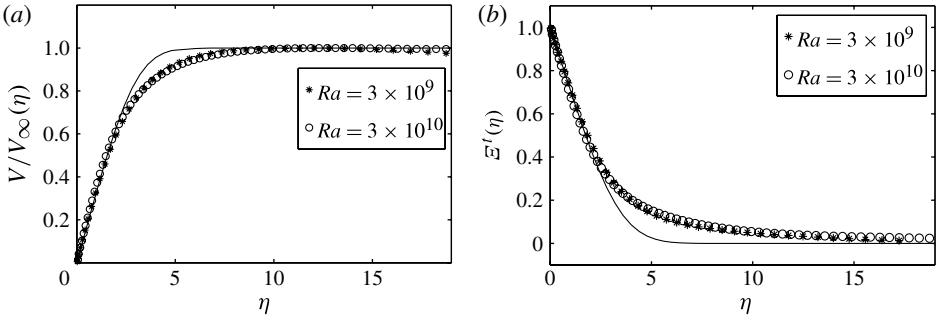

FIGURE 3. Mean profiles of (*a*) velocity and (*b*) temperature at probe array 1 for two different Rayleigh numbers. Quantities are the same as in figure 2. The solid lines in each figure correspond to the classical (*a*) Prandtl–Blasius and (*b*) Pohlhausen solutions.

a so-called dynamic rescaling of the boundary layer results in mean profiles that come closer to the Prandtl–Blasius–Pohlhausen predictions. As in the particle image velocimetry in the experiment, we analyse the fields in a small planar window. We take this window to be in the centre of the cylindrical cell. Zhou *et al.* (2011) found

that the boundary layer profiles come closer to the Prandtl–Blasius–Pohlhausen case downstream of the LSC. This plane is in our case also aligned for each snapshot with the direction of the instantaneous large-scale wind. This direction is determined by the angle ϕ_{LSC} defined in (3.8). The window has a width of $0.02R$, $0.1R$ or $0.4R$ starting from the centreline of the cell. In order to improve the statistics, we conduct this analysis at the top and bottom plates independently for each snapshot. This implies that the large-scale flow direction has to be determined separately at each plate. It is known that the large-scale circulation obeys a slightly twisted roll shape (Xi & Xia 2008*a*).

The instantaneous velocity boundary layer thickness $\delta_v(t)$ is determined to be the intersection point of the horizontal line through the first local maximum of the velocity profile and the tangent to the profile at the plates. The same procedure is repeated for the instantaneous thermal boundary layer thickness $\delta_T(t)$. Vertical distances have to be rescaled with

$$z_v^*(t) = \frac{z}{\delta_v(t)} \quad \text{and} \quad z_T^*(t) = \frac{z}{\delta_T(t)}. \tag{3.4}$$

The resulting velocity or temperature profiles follow by (Zhou & Xia 2010*a*)

$$V^*(z_v^*) = \langle V(r, \phi_{LSC}, z, t)|z = z_v^*\delta_v\,(t)\rangle_r, \tag{3.5}$$

$$\Xi^*(z_T^*) = \langle \Xi\,(r, \phi_{LSC}, z, t)|z = z_T^*\delta_T\,(t)\rangle_r\,. \tag{3.6}$$

Here $\langle\cdot\rangle_r$ indicates an averaging with respect to r in the plane that is aligned in ϕ_{LSC} and the rescaled temperature Ξ is taken at the bottom and top, respectively. The corresponding profiles are shown in figure 4(*a–c*). Contrary to the experiments by Zhou & Xia (2010*a*) and the two-dimensional DNS by Zhou *et al.* (2010, 2011), deviations from the Prandtl–Blasius–Pohlhausen profiles remain for all window widths and velocities used. A better agreement is, however, observable when the window is chosen to be narrower in radial extension. A further improvement for the width $0.4R$ is found when the radial component u_r is used instead of V defined in (3.1). For smaller windows, however, the agreement with respect to V was again better than for u_r. The deviations for the temperature are more persistent, which is caused by the plume detachments as we will see in § 4. We verified that the results are statistically converged by varying the number of samples. A shift of the window away from the centre of the plate or a combination of neighbouring windows with angles around ϕ_{LSC} did not lead to a better agreement with the predictions of Prandtl–Blasius–Pohlhausen theory. The same holds for window sizes smaller than $0.02R$.

A first significant difference to the previous analysis can, however, be identified immediately. In figure 4(*d*) we compare the mean of the velocity (u_r) in the analysis plane with the mean of the velocity (u_ϕ) perpendicular to the analysis plane with a window of width $0.4R$. It can be seen that the ratio takes a significant non-negligible value, in contrast to the two-dimensional and quasi-two-dimensional situations, respectively. At $z_v^* = 0.5$, the height for which the measured data start to differ from the theoretical profile, the ratio has increased to a value of 0.42. This is one important difference from the two-dimensional DNS and the quasi-two-dimensional laboratory measurements, and it gives a first hint as to why the deviations from the Blasius prediction persist in our geometry.

3.3. *Fluctuating boundary layer thickness*

Figure 5 shows time series of both thermal and velocity boundary layer thicknesses obtained from the time series at probe array 1. Shorter sequences of the same type

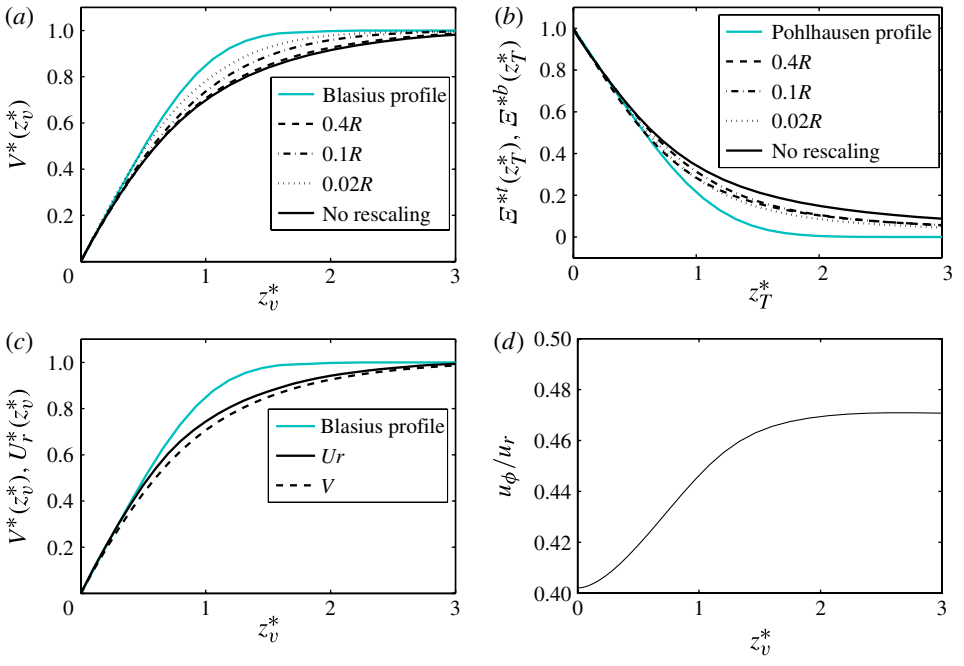

FIGURE 4. (Colour online) Dynamic rescaling of the mean profiles. (*a*) Dynamically rescaled mean velocity profile for different widths of the analysis plane. For comparison the Blasius profile and the profile without rescaling are added. (*b*) Dynamically rescaled mean temperature profile. Again, the Pohlhausen solution and the mean profile without rescaling are also shown. (*c*) Comparison of the rescaling of V^* as defined in (3.5) with $U_r^*(z_v^*) = \langle u_r(r, \phi_{LSC}, z, t)|z = z_v^*\delta_v\,(t)\rangle_r$ for a window of width $0.4R$. (*d*) Ratio of the mean velocities in the plane u_r and perpendicular to the plane u_ϕ for a window of width $0.4R$.

are obtained from the analysis in the planar observation window which is aligned with the instantaneous wind. We can see that both thicknesses fluctuate strongly for both Rayleigh numbers. Similar to the two-dimensional DNS of Zhou *et al.* (2010), the fluctuations of the velocity boundary layer thickness are slightly stronger than those of the thermal boundary layer. In particular, we observe rare large thickness events for the velocity which can be related to profiles that grow gradually from $z = 0$. We performed a Fourier analysis of both time series and could not detect a characteristic time scale, but a slowly decaying continuous spectrum which indicates a chaotic signal. The cross-correlation ratio, defined by (Zhou *et al.* 2010)

$$g(\tau) = \frac{\langle[\delta_v(t) - \langle\delta_v\rangle_t]\,[\delta_T(t+\tau) - \langle\delta_T\rangle_t]\rangle_t}{\sqrt{\langle[\delta_v(t) - \langle\delta_v\rangle_t]^2\rangle_t}\sqrt{\langle[\delta_T(t) - \langle\delta_T\rangle_t]^2\rangle_t}}, \tag{3.7}$$

is plotted in figure 6 for the fluctuating boundary layer thicknesses at the bottom plate. The symbol $\langle\cdot\rangle_t$ denotes a time average. Compared to two-dimensional DNS at $Pr = 0.7$ (Zhou *et al.* 2010), the variation of the function $g(\tau)$ is much less regular. In both of our cases the peak is slightly shifted to the left of zero, which would indicate that variations of the thermal boundary layer cause variations of the velocity boundary layer. The lead time is, however, shorter than the time that we will identify as the time span for a plume detachment. The correlations between both fluctuating boundary

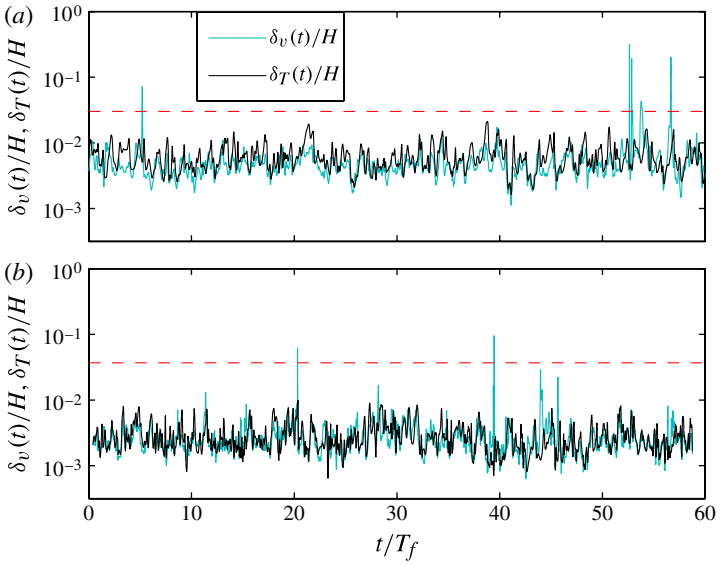

FIGURE 5. (Colour online) Fluctuation of the instantaneous thickness of the velocity and thermal boundary layers as formed at the centre of the top plate of the cell. (*a*) $Ra = 3 \times 10^9$, (*b*) $Ra = 3 \times 10^{10}$. The dashed lines in both figures mark the end of probe array 1 at which the data are taken for both Ra. Thickness values that exceed this height are related with velocity profiles that grow gradually from $z = 0$ and therefore an intersection point with the horizontal line through the first local maximum that lies beyond the end of the probe array.

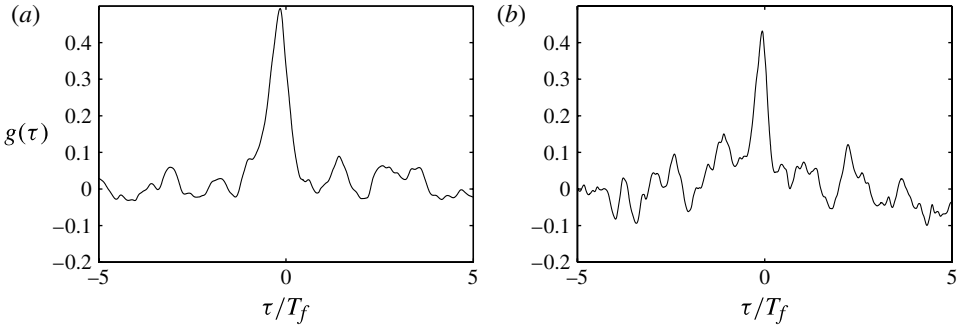

FIGURE 6. Cross-correlation ratio as given in (3.7) for the time series of the instantaneous boundary layer thickness at the bottom plate. (*a*) $Ra = 3 \times 10^9$ with approximately 57 000 data points. (*b*) $Ra = 3 \times 10^{10}$ with approximately 23 000 data points. The outliers from figure 5, i.e. the points that exceed the dashed lines, have been excluded from the analysis.

layers are less pronounced than in the two-dimensional studies. We conclude that such behaviour is due to the three-dimensional nature of the boundary layer dynamics. We also tried to conduct a similar analysis for the data in the small planes which are aligned with the instantaneous large-scale wind. The number of samples was, however, too small for a reliable cross-correlation analysis.

To extract a characteristic time scale from the time series data, we analyse the variations of boundary layer thicknesses about their means, to determine the average

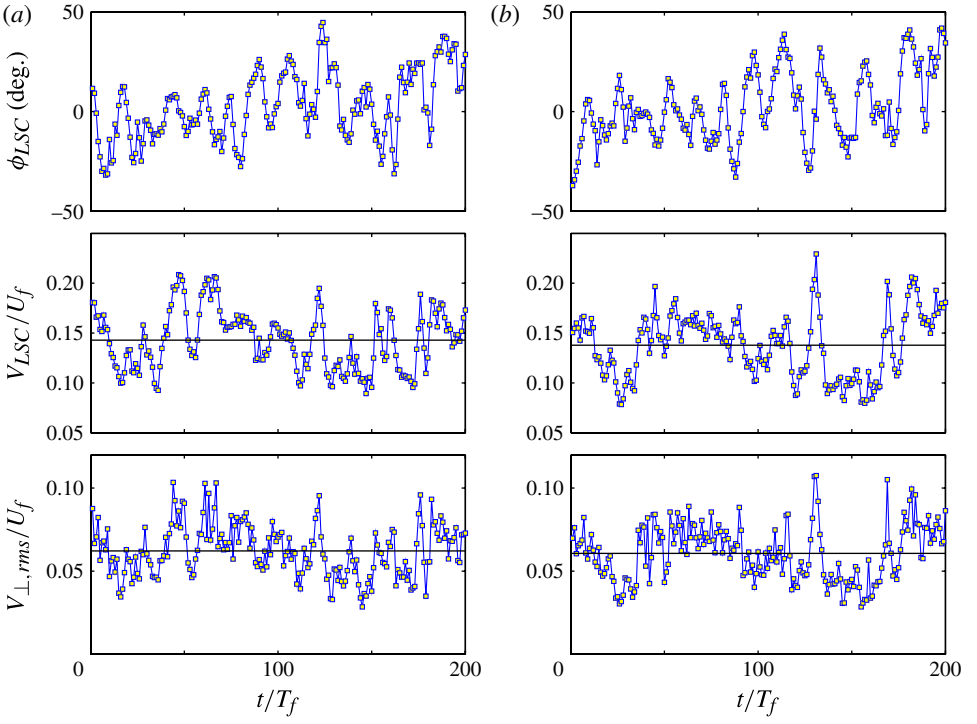

FIGURE 7. (Colour online) Direction, magnitude and r.m.s. of the velocity perpendicular to the instantaneous large-scale circulation. Quantities are denoted by ϕ_{LSC}, V_{LSC} and $V_{\perp,rms}$. (*a*) Top plate, (*b*) bottom plate. Data correspond to the analysis in figure 4 and are determined at $z = \delta_T$ for the bottom plate and at $z = H - \delta_T$ for the top plate, respectively. Data are for $Ra = 3 \times 10^9$. The solid horizontal lines indicate the means of the time series.

time intervals of $\delta_v(t)$ or $\delta_T(t)$ to cross their corresponding means. Our data for $Ra = 3 \times 10^9$ indicate that this interval for each boundary layer is about $T_{cross} \approx 0.5T_f$, which will turn out to be the time lag for a plume detachment in a local region close to the plate. We also repeated the analysis independently for the top boundary layers and reproduced this result. A characteristic variation time of the boundary layer is thus $2T_{cross} \approx T_f$. This time can be interpreted as the time at which plumes detach in a local region close to the plates (see also our analysis in the next section). It is short when compared to the average loop time of Lagrangian tracers in such a cell of approximately $20\,T_f$ (as found in Emran & Schumacher 2010), which is a characteristic loop time of the LSC.

3.4. *Fluctuations of the large-scale circulation in the convection cell*

Figure 7 displays the direction (or the angle of orientation) and magnitude of the LSC. The orientation of the LSC is used for the dynamical rescaling of the boundary layer profiles. One can see that the orientation of the mean flow at the same instant is different at the bottom plate compared to the top plate, supporting the idea of a twisted circulation roll (Funfschilling & Ahlers 2004; Xi & Xia 2008*a*,*b*). The instantaneous direction, ϕ_{LSC}, and the magnitude of the large-scale circulation, V_{LSC},

are determined by

$$\phi_{LSC}(t_0) = \left\langle \arctan \frac{u_y(x, y, z_0, t_0)}{u_x(x, y, z_0, t_0)} \right\rangle_{A_r}, \tag{3.8}$$

$$V_{LSC}(t_0) = \left\langle \sqrt{u_x(x, y, z_0, t_0)^2 + u_y(x, y, z_0, t_0)^2} \right\rangle_{A_r}, \tag{3.9}$$

where the subscript A_r denotes the average over a circular cross-section with $r \leqslant 0.88R$ at $z_0 = \delta_T$ for the bottom or $z_0 = H - \delta_T$ for the top plate. Furthermore we show the root-mean-square of the velocity vector, which is perpendicular to $\boldsymbol{v} = u_x \boldsymbol{e}_x + u_y \boldsymbol{e}_y$. This cross-flow velocity vector is determined by the relation $\boldsymbol{v}_\perp \cdot \boldsymbol{v} = 0$ at each point $(x, y, z_0) \in A_r$. The quantity is given by

$$V_{\perp,rms}(t_0) = \sqrt{\langle v_\perp^2(x, y, z_0, t_0)\rangle_{A_r}}. \tag{3.10}$$

It is seen that the circulation varies strongly in both amplitude and angle. In the case of the angle we do observe a fast variation of the orientation over a range of approximately 50°. On average the LSC is almost perfectly aligned with the x-axis ($\phi = 0$) along which we have positioned the probe arrays 1, 2 and 4. The amount of fluctuation perpendicular to the large-scale wind velocity is also significant, and reaches up to 50 % of V_{LSC}. The mean magnitude of V_{LSC} can be used to estimate an LSC turnover time by $\tau_{LSC} = \overline{V}_{LSC}^{-1} \times 2\pi(H/2) \approx 21 T_f$, which is close to the estimate from previous Lagrangian studies, as mentioned at the end of § 3.3 (Emran & Schumacher 2010). It is also consistent with an LSC turnover time of $18\,T_f$ (which corresponds to 35 s) in the Barrel of Ilmenau. Furthermore, Ahlers *et al.* (2009*a*) report a time scale of 25 s from their helium experiment at $\Gamma = 1/2$, which can be converted into 33 s by multiplication with 4/3 for a unit aspect ratio cell.

Superimposed on the fast oscillation is a very slow drift of the angle (see panels in the upper row of figure 7). This indicates that a small fraction of a very slow precession of the large-scale circulation is being observed. This slow mode can be present since the mean orientation of the roll is not locked in one particular direction, as is frequently observed in experiments. We are, however, not able to study this slow mode of motion in our DNS since it would exceed our present numerical capabilities in terms of the length of the simulation. Better access to this very slow large-scale dynamics would require investigation with low-dimensional models (Brown & Ahlers 2009) or models obtained by proper orthogonal decomposition of the turbulence fields (Bailon-Cuba & Schumacher 2011).

3.5. *Pressure gradient and temperature fluctuations in the boundary layer*

Figure 8 shows the temperature, the related temperature fluctuations, which are given by

$$T'(\boldsymbol{x}, t) = T(\boldsymbol{x}, t) - \langle T(z)\rangle_{A,t}, \tag{3.11}$$

and the magnitude of the horizontal pressure gradient (figure 8*c*), which is given by

$$\Pi = \sqrt{\left(\frac{\partial p}{\partial r}\right)^2 + \left(\frac{1}{r}\frac{\partial p}{\partial \phi}\right)^2}. \tag{3.12}$$

Data are taken at the edge of the boundary layer in the plane at $z = \delta_T$ at a time instant of the DNS run at $Ra = 3 \times 10^9$. The contours of Π, which are plotted in units

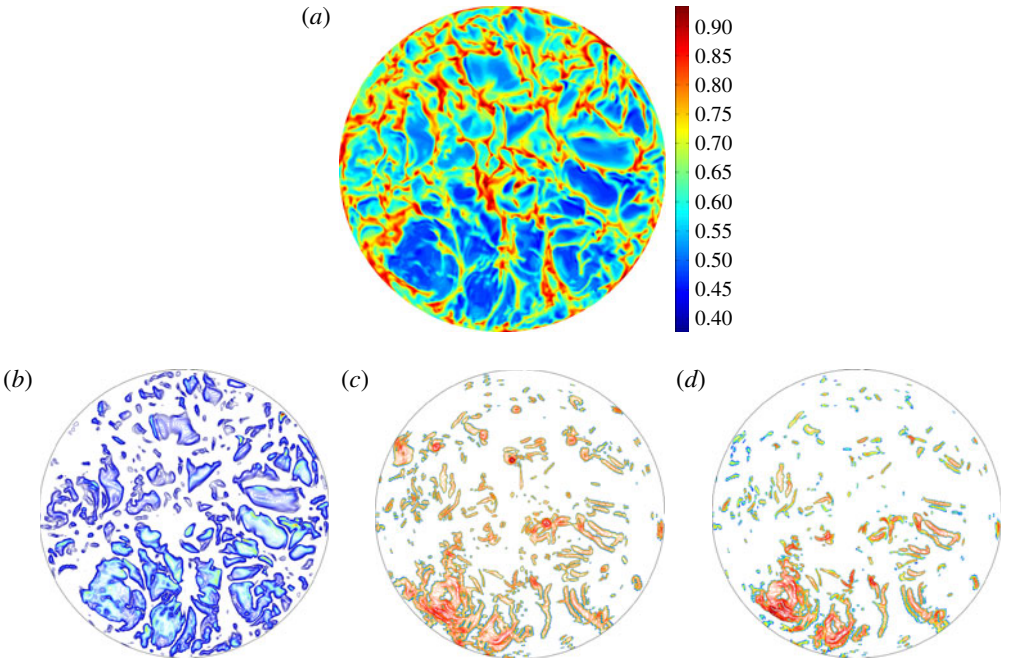

FIGURE 8. Spatial correlation between the horizontal pressure gradient and temperature. (*a*) A horizontal cross-section of temperature T. The three contour plots below show (*b*) the thresholded temperature fluctuations T_c', (*c*) the pressure gradient magnitude Π_c, and (*d*) the product of both. Data are for $Ra = 3 \times 10^9$ and taken at $z = \delta_T$. Pressure gradient magnitude and product are shown in logarithmic units.

of the logarithm to the base of 10, imply that the pressure field varies strongly in the horizontal plane at this height. In more detail, we display in figure 8 the quantity

$$\Pi_c(\boldsymbol{x}, t) = \Pi(\boldsymbol{x}, t)\, \Theta(\Pi - C), \tag{3.13}$$

with the Heaviside function Θ and a threshold C. The pressure field in the incompressible flow limit is directly connected with the flow, and thus reflects the high spatial (and temporal) variability of the flow, including the large-scale circulation as analysed in figure 7.

Theerthan & Arakeri (1998) and Puthenveettil & Arakeri (2005) have discussed in detail that the horizontal pressure differences are an essential driver of the velocity inside the boundary layer. In figure 9 we compare vertical profiles taken with respect to time and different horizontal cross-sections $A = \pi r^2$. Averages of the radial component of the pressure gradient $\langle \partial p/\partial r \rangle_{A,t}$ and the Reynolds stress $\langle u_r' u_z' \rangle_{A,t}$ are shown as examples. The pressure gradient component is non-negligible in the boundary layer. As in van Reeuwijk *et al.* (2008*b*), we compare here the ratio

$$\gamma = \frac{\left| \displaystyle\int_0^{\delta_v} \langle \partial p/\partial r\,(z) \rangle_{A,t}\, \mathrm{d}z \right|}{|\, \langle u_r' u_z' \rangle_{A,t}\, |_{\delta_v}}. \tag{3.14}$$

Note that both terms contribute to the friction factor. Values of $\gamma = 1.16$, 1.77 and 5.21 were obtained for cross-sections A with radius R, $R/2$ and $R/5$. We thus confirm

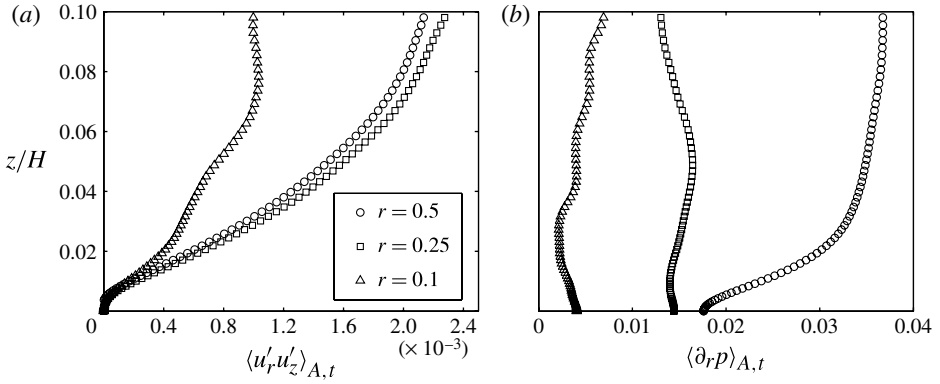

FIGURE 9. Vertical mean profiles of (a) the Reynolds stress, and (b) the radial derivative of pressure obtained over different horizontal cross-sections. The full circular cross-section A of the cylindrical cell with $r = 0.5$ (or $r = R$) is compared with smaller cross-sections A that have half and one-fifth of the radius, all of which are concentric with respect to the centreline. Data are for $Ra = 3 \times 10^9$ and in units of U_f^2 and U_f^2/H.

their finding that this ratio is significant even in a central region where the data come closest to the Blasius profiles. We recall that the pressure gradient would be zero in the Blasius case.

When the spatial support of Π_c is compared with the temperature distribution in the same horizontal plane (see figure 8b–d), we observe that maxima of Π are found mostly in the low-temperature voids between the skeleton of plumes, i.e. in regions which are given by $T' < 0$ (see figure 8b) or

$$T'_c(\boldsymbol{x}, t) = T'(\boldsymbol{x}, t)\, \Theta(-T'). \tag{3.15}$$

Again, we use the Heaviside function Θ. In regions of high pressure gradient the horizontal flow will be accelerated, and piles up local plumes that eventually detach from the boundary layer. The spatial correlation becomes directly visible when both thresholded fields Π_c and T'_c are multiplied as shown in figure 8(d). The area covered by these correlated regions is $\sim$11 % of the total area, and remained nearly constant in time, which we verified by a pressure field snapshot analysis over a few free-fall time units in the case of $Ra = 3 \times 10^9$.

It is also observed from figure 8(a) that the plumes are line-like, but with significant thickness modulations along their stems. At Prandtl number 0.7 and for the present Rayleigh numbers, diffusion still plays an important role in the plume formation. This will, in our view, also result in limited applicability of two-dimensional plume models, in which spatial variations in the third direction are assumed to be small (e.g. Puthenveettil & Arakeri 2005). Similar temperature patterns have been found in Zhou, Sun & Xia (2007), Shishkina & Wagner (2008), Zhou & Xia (2010b) and Puthenveettil *et al.* (2011), where length, width and aspect ratio of the filaments in this skeleton of plumes have been quantified in detail.

Figure 10 displays the probability density function (p.d.f.) of the two components of the pressure gradient in two planes parallel to the bottom plate. This figure underlines the findings from figure 8. The fluctuations of the pressure gradient across the boundary layer are highly intermittent, as shown by the stretched exponential p.d.f.s of the both components. Emran & Schumacher (2008) have studied the statistics of the

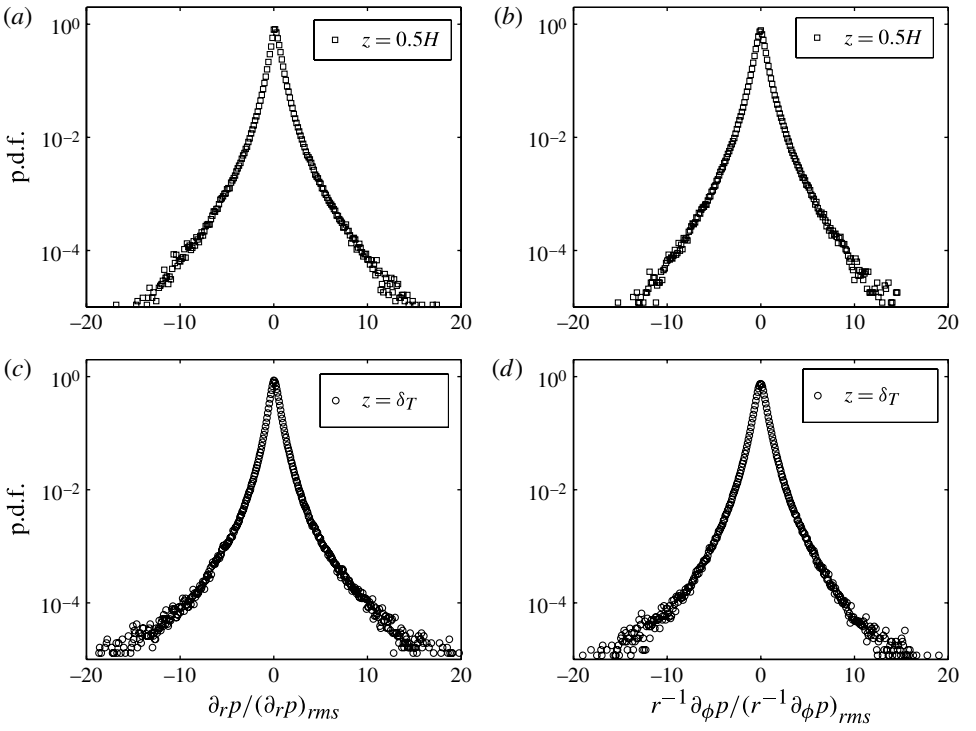

FIGURE 10. Probability density functions of the two horizontal components of the pressure gradient. (*a,c*) $\partial p/\partial r$ in the centre plane of the cell and at the top of the boundary layer, (*b,d*) $r^{-1}\partial p/\partial\phi$. Data are for $Ra = 3 \times 10^9$.

temperature field and its gradients in detail. The spatial variations of the temperature, as quantified by the statistics of the temperature gradient components as well as the thermal dissipation rate, were found to obey the strongest spatial intermittency in the boundary layer. The intermittency of the pressure gradient field shows qualitatively the same behaviour: it is enhanced in the boundary layer.

We summarize our boundary analysis at this point. The numerical data demonstrate that significant differences from the classical Prandtl–Blasius–Pohlhausen theory are present in comparison to the two-dimensional case and the quasi-two-dimensional experiments. The near-wall flow and temperature structures are three-dimensional and unsteady, as is the large-scale circulation to which the boundary layer dynamics is coupled. This is in line with a fluctuating large-scale circulation and the horizontal pressure gradient in the cylindrical cell.

4. Comparison with laminar boundary layers of mixed convection

4.1. *Two-dimensional boundary layer theory of mixed convection*

As already discussed in the Introduction, the boundary layer in turbulent convection can be considered as mixed type, i.e. driven by the natural convection and also by the LSC. In classical boundary layer theory, both limiting cases have been studied to some extent. These are the purely forced convective flow, also known as the classical Prandtl–Blasius–Pohlhausen case (Blasius 1908; Pohlhausen 1921), and the purely natural convective flow (Stewartson 1958; Rotem & Claassen 1969). For

mixed convection, the Boussinesq equations of motion (2.1)–(2.3) are reduced to the following set of two-dimensional and steady boundary layer equations (Schlichting 1957):

$$u_x\frac{\partial u_x}{\partial x}+u_z\frac{\partial u_x}{\partial z}=-\frac{\partial p}{\partial x}+\nu\frac{\partial^2 u_x}{\partial z^2}, \tag{4.1}$$

$$0=-\frac{\partial p}{\partial z}+\alpha g T, \tag{4.2}$$

$$\frac{\partial u_x}{\partial x}+\frac{\partial u_z}{\partial z}=0, \tag{4.3}$$

$$u_x\frac{\partial T}{\partial x}+u_z\frac{\partial T}{\partial z}=\kappa\frac{\partial^2 T}{\partial z^2}. \tag{4.4}$$

The corresponding dimensionless parameters are the Reynolds and Grashof numbers of the problem, which are given by

$$Re_x=\frac{V_\infty x}{\nu},\quad Gr_x=\frac{g\alpha(T_w-T_\infty)x^3}{\nu^2}. \tag{4.5}$$

At the plate ($z=0$), the boundary conditions are $T=T_w$ and $u_x=u_z=0$. Far away from the plate ($z\to\infty$), it follows that $T=T_\infty$ and

$$u_x(z\to\infty)=\begin{cases}V_\infty & \text{for forced convection,}\\ 0 & \text{for natural convection.}\end{cases} \tag{4.6}$$

In both cases one can define similarity variables η and parameters ϵ for the perturbation expansion of mixed convection. In agreement with the definitions (3.1)–(3.3) we can proceed as follows. Starting from purely forced convection, the expansion reads (Sparrow & Minkowycz 1962)

$$\frac{u_r(x,z)}{V_\infty}=f_0'(\eta)+\epsilon f_1'(\eta)+\cdots, \tag{4.7}$$

$$\Xi(x,z)=\frac{T(x,z)-T_\infty}{T_w-T_\infty}=\theta_0(\eta)+\epsilon\theta_1(\eta)+\cdots, \tag{4.8}$$

while starting from purely natural convection, it reads (Stewartson 1958)

$$\frac{u_r(x,z)}{V_n(x)}=g_0'(\eta)+\epsilon g_1'(\eta)+\cdots, \tag{4.9}$$

$$\Xi(x,z)=\frac{T(x,z)-T_\infty}{T_w-T_\infty}=\chi_0(\eta)+\epsilon\chi_1(\eta)+\cdots, \tag{4.10}$$

where functions with index 0 represent the unperturbed velocity components or temperature. Furthermore $V_n(x)=(\nu g^2\alpha^2\,(T_w-T_\infty)^2\,x)^{1/5}$. More details are provided in the Appendix for completeness. The resulting systems of perturbation equations for the boundary value problems can be solved by a shooting method using a fourth-order Runge–Kutta scheme (Hieber 1973).

Figure 11 shows the resulting mean streamwise flow and temperature profiles for the case of $Pr=0.7$. The perturbation expansion has been carried out to first order only, and curves are plotted for different magnitudes of ϵ as given in (A 2). Several aspects can be observed. The boundary layer flow is accelerated if buoyancy effects

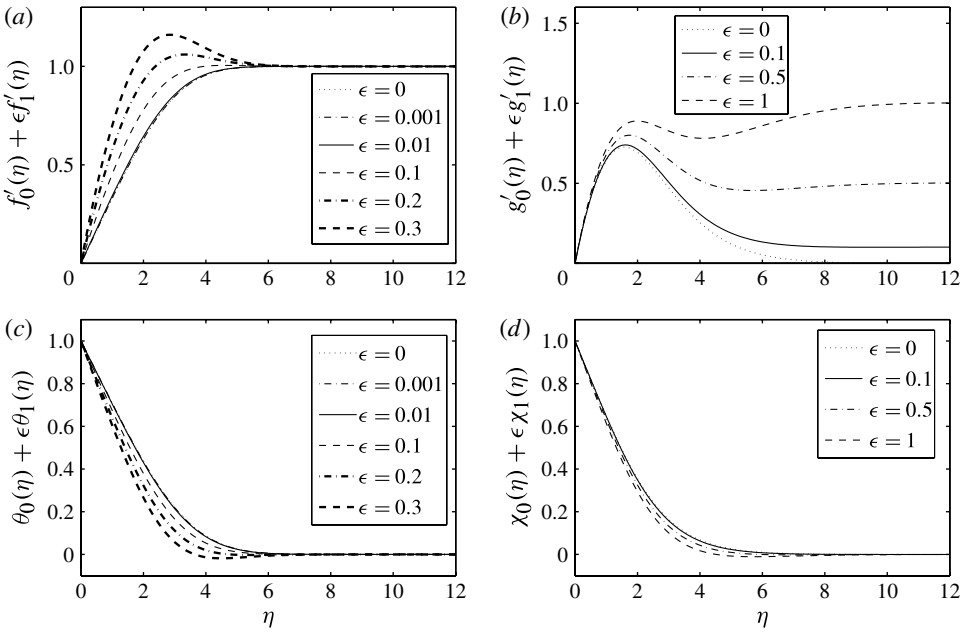

FIGURE 11. Vertical profiles of the normalized downstream velocity and temperature resulting from a first-order perturbative expansion of (*a,c*) forced, and (*b,d*) natural convection. The values of the expansion parameter ϵ are indicated in the legend. The similarity variables are given by (A 1). We also show examples for ϵ unrealistically large, in order to indicate the deviations better.

are added to the classical Blasius case, as seen in figure 11(*a*). The same holds if a purely natural convection layer is also driven by an outer flow such as the large-scale circulation in the present system (seen figure 11*b*). The imposed outer flow causes a significant variation in the velocity profile. The modifications in the temperature are less pronounced. In both cases the resulting mean temperature profiles deviate slightly from the unperturbed results.

Let us now estimate the Rayleigh number dependence of the boundary layer thicknesses in both limiting cases of laminar boundary layers. The dependence of the thickness on the Reynolds number in forced convection is given by (Schlichting 1957)

$$\delta_v \sim \frac{x}{Re_x^{1/2}}. \tag{4.11}$$

By using a scaling relation between Reynolds and Rayleigh numbers for convection at $Pr \approx 1$ and $\Gamma = 1$, which is taken from Ahlers *et al.* (2009*b*), namely $Re \sim Ra^{0.45}$, this results in a Rayleigh number dependence $\delta_v \sim \delta_T \sim Ra^{-0.22}$ in the purely forced convection case. In a natural convection boundary layer, the Grashof number is substituted by the Reynolds number, and with the similarity variable $\eta = zGr_x^{1/5}/x$ one obtains

$$\delta_T \sim \frac{x}{Gr_x^{1/5}}. \tag{4.12}$$

Again, we are interested in convection with Prandtl numbers around one such that $Gr_x \approx Ra$. It follows that $\delta_v \sim \delta_T \sim Ra^{-0.2}$, which is very close to the forced case. Both

scaling estimates suggest that the differences in the Rayleigh number dependence of the boundary layer thicknesses are rather small when both limits – natural and forced convection – are compared. With only two runs at different Rayleigh numbers, we are not able to conduct scaling laws of the thicknesses with respect to Ra.

4.2. *Boundary layer dynamics in a small observation window*

The present direct numerical simulations give us the opportunity to zoom into the boundary layer dynamics at higher Rayleigh numbers, and to test how closely the local profiles match the results of the classical boundary layer theories that we have just discussed. Out of the comprehensive data record, we have picked two characteristic dynamic sequences of the boundary layer structures: a plume detachment event and the post-plume-detachment phase for which the boundary layer relaminarizes. Each of these typical sequences covers a time lag of $\sim 0.45 T_f$ for our data at each Rayleigh number. We consider them to be the two essential building blocks of the boundary layer dynamics. In order to connect with classical boundary layer theory, we analyse the fields again in a small vertical observation plane that is aligned with the instantaneous large-scale circulation. Our observation window has a size of length $\times$ height equal to $9\delta_T \times 9\delta_T$ for $Ra = 3 \times 10^9$ and $19\delta_T \times 19\delta_T$ for $Ra = 3 \times 10^{10}$. The dense temporal output of the data spans $35 T_f$ for $Ra = 3 \times 10^9$ and $5 T_f$ for $Ra = 3 \times 10^{10}$ with a time interval of $0.05 T_f$ in each run.

A typical plume detachment event is seen in figure 12, where the temperature is shown in figure 12(*a,d,g*), the velocity field (u_r, u_z) projected into the plane in figure 12(*b,e,h*) and the out-of-plane velocity component u_ϕ in figure 12(*c,f,i*), respectively. The rise of the hot fluid causes strong upward outflow that is connected with the plume detachment. This is in line with a strong inflow in the back of the plume due to the incompressibility of the flow. The whole detachment process is accompanied by a cross-wind underlining the three-dimensionality of the whole dynamical process. The magnitude of the azimuthal velocity is comparable with the amplitudes of $V_{\perp,rms}$ in figure 7. Furthermore, the largest amplitudes of the azimuthal velocity component are found to be in line with the largest values of $\delta_v(t)$ and $\delta_T(t)$. The plume detachment is thus one of the dynamical processes that cause the fluctuations of the boundary layer thicknesses. Our snapshot analysis also showed that the thickness variations are not significantly delayed with respect to each other, which is in line with the short lead time for $g(\tau)$ which we discussed in § 3.3. The significant azimuthal velocity component confirms previous observations by Shishkina & Wagner (2008) that a strong local vorticity vector field is aligned with a line-like plume ridge.

The corresponding mean profiles of all velocity components and the temperature are shown in figure 13(*a*). They are obtained by averaging in the observational window with respect to the radial direction. The detachment is accompanied by a deceleration of the radial velocity and strong upward and downward flows into the bulk region as already described above. The temperature profiles deviate significantly from the classical laminar boundary layer profile (see figure 11) as the hot fluid parcel leaves the observation area.

The ambient post-plume-detachment phase is illustrated in figure 14. At first glance the flow and temperature fields seem to agree much better with the predictions from the laminar boundary layer theory. However, not too far away from the wall, non-negligible upward and downward flows are still present. The stratification of the temperature field is nearly unperturbed and the azimuthal component is more homogeneously distributed over the window in comparison to the detachment phase. This also becomes obvious from the plots in figure 13(*b*), where the temperature

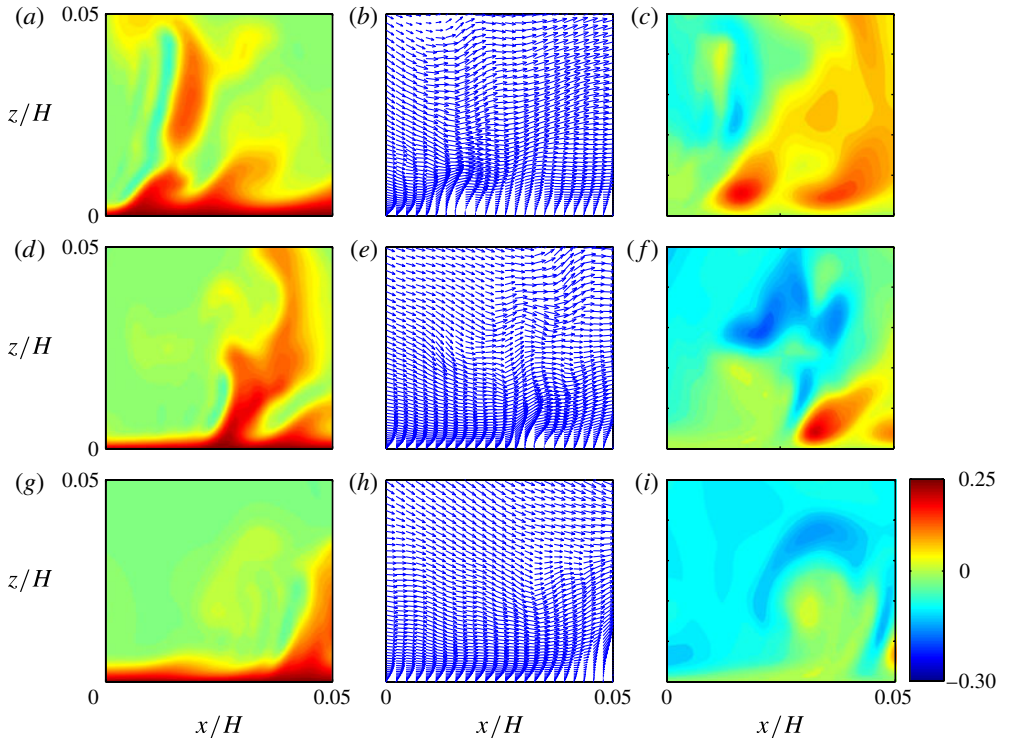

FIGURE 12. Sequence of three vertical planar cut snapshots to illustrate the detachment of a plume. (*a,d,g*) Contours of the temperature T, (*b,e,h*) vector plot of (u_r, u_z), and (*c,f,i*) contours of u_ϕ. Images (*d–f*) and (*g–i*) lag behind images (*a–c*) by $0.2T_f$ and $0.4T_f$, respectively. The colour legend (not shown here) for the temperature in (*a,d,g*) corresponds to an equidistant colour scale between zero and one. Scalar magnitudes for the azimuthal velocity component are indicated by the colour bar in (*c,f,i*). The three time instants are numbers 1, 5 and 9 out of a sequence of nine equidistant snapshots. Data are for $Ra = 3 \times 10^9$, where $\delta_T/H = 0.0057$.

profiles are much less perturbed than in a plume detachment phase. Nevertheless, even in this phase the flow is three-dimensional, as we can see from the profiles of the azimuthal velocity component. Recall that the observational window in figures 12 and 14 has a height of $0.05H$. Up to this distance from the wall, the maximum magnitude of the mean vertical velocity component is much smaller.

The radial velocity and temperature profiles in both sequences indicate that the profiles vary strongly, even over such a short dynamic sequence. The velocity is strongly enhanced in the boundary layer, as it also results from the two-dimensional perturbative analysis, such as in the forced case (see figure 11*a*). Furthermore, the presented data indicate that the large-scale circulation is always strong enough such that pure natural convection with a streamwise velocity that goes to zero is not established (see figure 11*b*).

We repeated this analysis for the second run at $Ra = 3 \times 10^{10}$. The qualitative picture remains unchanged for each phase, the plume detachment period and the post-plume phase. Note that the mean advection direction of the plumes is now opposite. The data are shown in the same way as for the lower Rayleigh number in figures 15 and 17.

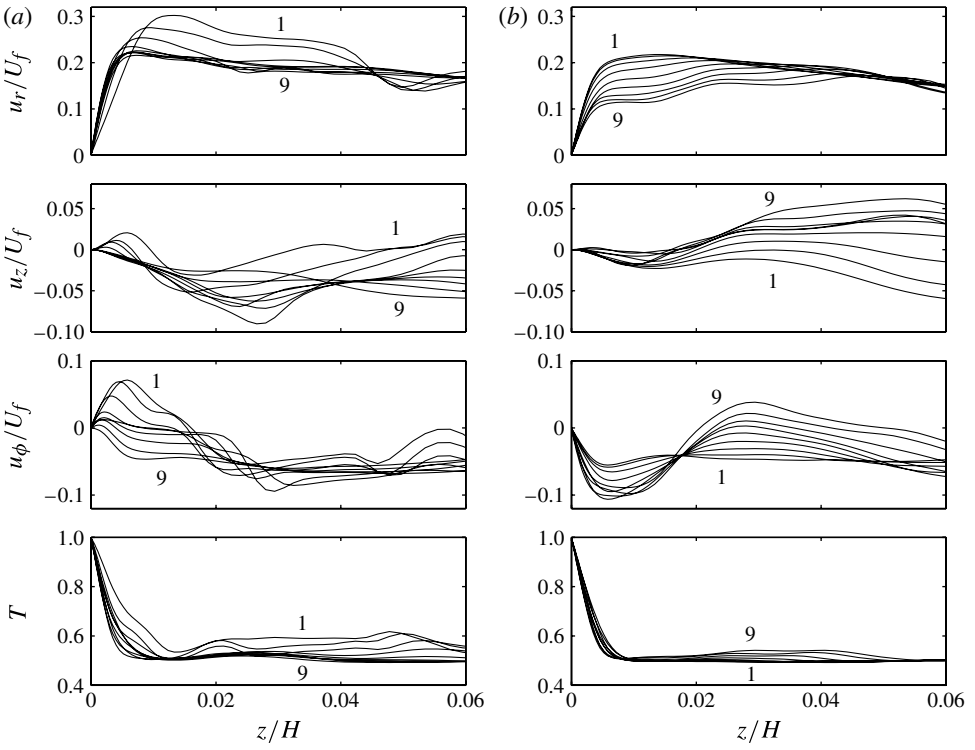

FIGURE 13. Sequence of nine profiles that correspond to (*a*) the data of figure 12 for the plume detachment phase and (*b*) the data of figure 14 for the post-plume phase. They are obtained by an averaging in radial (or *x*-) direction over the window that is shown in figure 12. From top to bottom: radial velocity component u_r/U_f, vertical velocity component u_z/U_f, azimuthal velocity component u_ϕ/U_f, and temperature T.

As expected, the detaching plumes are more filamented and the boundary layer in the post-plume phase is thinner. The amplitude of the azimuthal velocity component remains significant, as seen in figure 16.

In both runs the profiles of u_ϕ show the following behaviour in the vicinity of the wall. In the plume detachment phase this velocity component changes sign when moving forward in time from snapshot one to nine. This is not the case in the post-plume phase. The differences between the temperature profiles for each phase are even more pronounced in comparison to the lower Rayleigh number run.

The time lags of the plume detachment and post-plume phases have been calculated as follows. We take the radially averaged temperature field at $z \approx 5\delta_T$ for each snapshot in the window. If this value exceeds the mean bulk temperature, it is assigned with a detachment event; otherwise it belongs to the post-plume phase. By applying this simple procedure, the time series is digitalized. The resulting step function has shorter and longer time periods for each dynamical building block. The mean time of plume detachment and post-plume is about the same, and gives about $0.45T_f$ for $Ra = 3 \times 10^9$ where we had a sufficiently long time series. Combining both gives a typical cycle time of T_f, which is consistent with the $2T_{cross}$ from the fluctuating boundary layer thickness in § 3.4.

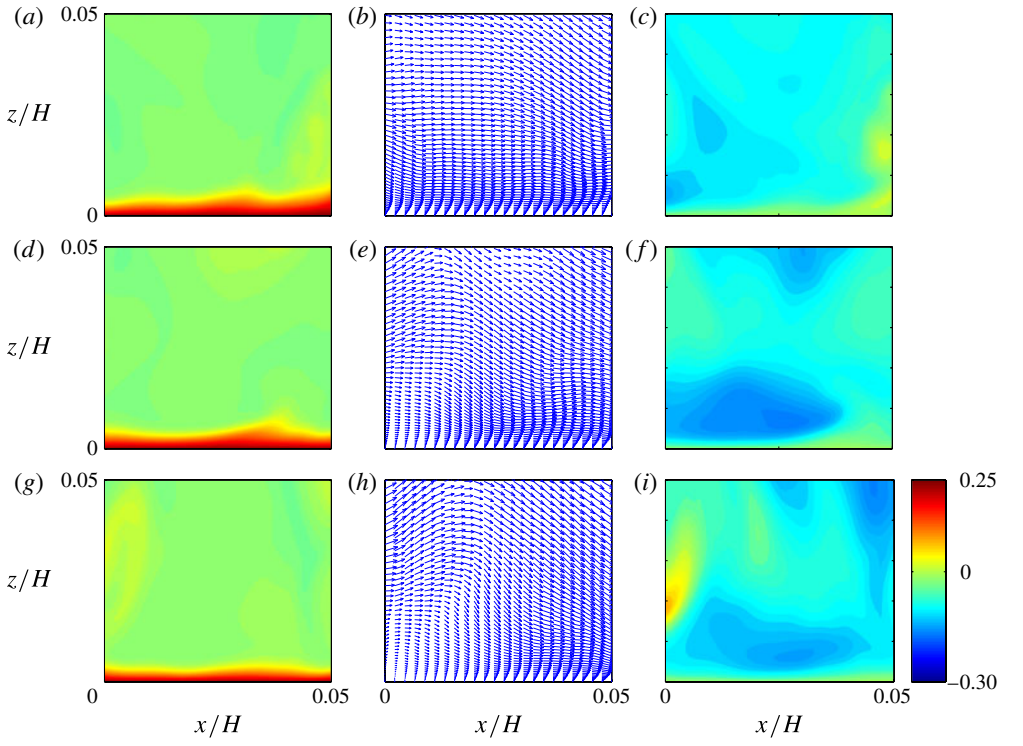

FIGURE 14. Sequence of three vertical planar cut snapshots to illustrate the phase after the detachment of a plume. (*a,d,g*) Contours of the temperature T, (*b,e,h*) vector plot of (u_r, u_z), and (*c,f,i*) contours of u_ϕ. Images (*d–f*) and (*g–i*) lag behind images (*a–c*) by $0.2T_f$ and $0.4T_f$, respectively. The colour legend (not shown here) for the temperature in (*a,d,g*) corresponds to an equidistant colour scale between zero and one. Scalar magnitudes for the azimuthal velocity component are indicated by the colour bar in (*c,f,i*). The three time instants are numbers 1, 5 and 9 out of a sequence of nine equidistant snapshots. Data are again for $Ra = 3 \times 10^9$.

In figures 18 and 19 we try to match the time-averaged profiles obtained from the short dynamic sequences with the predictions from the mixed convection boundary layer theory including the first-order perturbation. Our profiles again display the features we detected in the original time series analysis over much longer time intervals (see figure 3). However, we can now trace the slower increase of the temperature profile clearly back to the plume detachment events. Similar connection holds for the velocity profile in the post-plume-detachment phase. The local dynamical behaviour suggests that the three-dimensional large-scale circulation is now connected to the boundary layer section. Inflows from the top of our observation window are observed, which cause large variations in the velocity profiles. These variations reach the same magnitude as in the plume detachment phase and manifest in the deviations for velocity profile $\langle u_r \rangle_r$ in the observation plane (see figure 19). We have thus shown that the simulation data combine elements of forced and natural convection. Neither in the plume detachment nor in the post-plume phase can the theoretical profiles of both the temperature and velocity fields be perfectly matched to the data. The dynamics close to the walls is always three-dimensional.

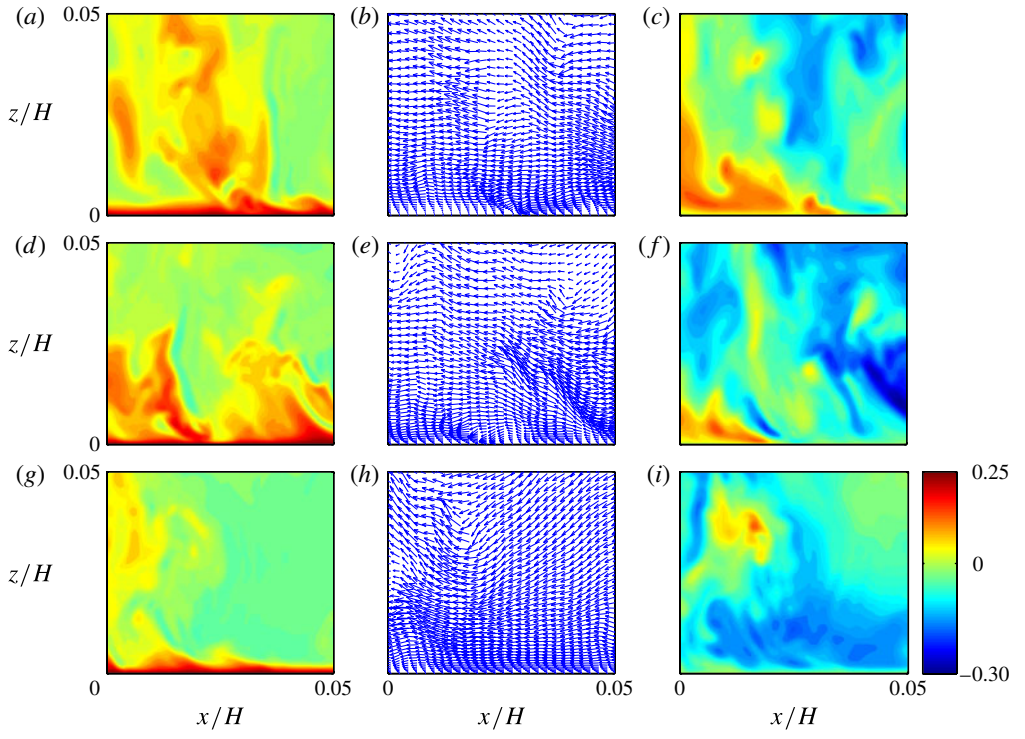

FIGURE 15. The same sequence of contour plots as in figure 12 for $Ra = 3 \times 10^{10}$, where $\delta_T/H = 0.0026$.

5. Summary and outlook

We have studied the boundary layer dynamics of three-dimensional turbulent Rayleigh–Bénard convection in a cylindrical cell of aspect ratio one for Rayleigh numbers larger than 10^9. Our studies are focused on the convection in air with $Pr = 0.7$. The simulations provide access to the full spatial and temporal information inside and outside the thermal and velocity boundary layers.

The large-scale circulation in the cell varies significantly in direction and amplitude, providing time-dependent driving of the boundary layer dynamics. The fluctuating LSC is in line with a strongly fluctuating thickness of both boundary layers which can be defined from instantaneous snapshots, as suggested by Zhou & Xia (2010*a*). When these fluctuations are incorporated into a dynamical rescaling, the matching of the mean profiles to Prandtl–Blasius–Pohlhausen theory improves. However, in the present cylindrical cell, deviations from the classical Prandtl–Blasius–Pohlhausen profiles will remain, in particular for temperature. Further, the profiles do not fit the other limiting case of natural convection.

In the present DNS we aimed at connecting dynamical behaviour in the boundary layer with the observed statistics. Our analysis found that the boundary layers follow a three-dimensional dynamics in all dynamical phases. This conclusion results from investigations of the pressure, the LSC and local dynamic sequences. Pressure gradient components and temperature fluctuate strongly and follow non-Gaussian statistics. A significant flow perpendicular to a two-dimensional analysis plane is present during

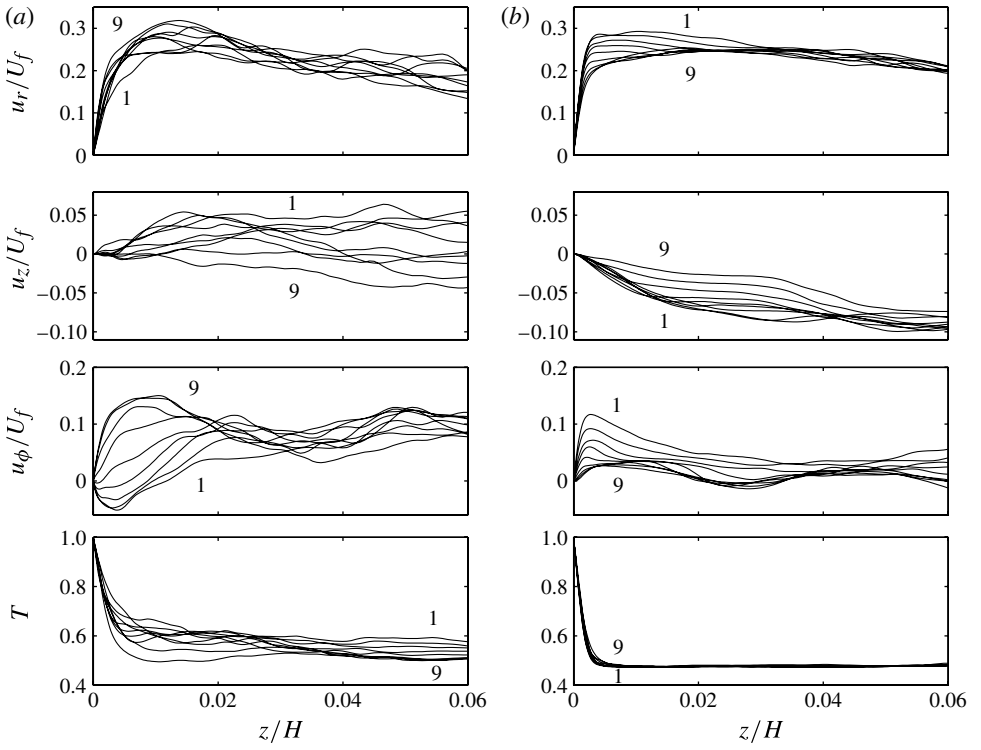

FIGURE 16. Sequence of nine profiles that correspond to (a) the data of figure 15 and (b) the data of figure 17. All data are given in the same units as discussed in figure 13.

detachment; it is also observed in the post-detachment phase. These plumes form a line-like skeleton, but are not found to be aligned in parallel. Their detachment is accompanied with a significant variation of the boundary layer thicknesses and a cross-wind (azimuthal velocity) with a significant amplitude.

All these observational outcomes violate the assumptions made in deriving the similarity solutions in the classical boundary layer theories. Analyses in a pointwise probe array as well as in a observational window support our findings. This also limits the applicability of two-dimensional plume models and, in our view, causes the deviations from both the classical Prandtl–Blasius–Pohlhausen and natural convection cases. It can be expected that the dynamics in the boundary layer will become increasingly intermittent when the Rayleigh number grows, a point that needs to be investigated further. Such increasingly intermittent behaviour would be typical for a transitional boundary layer which is ultimately evolving towards a turbulent one at larger Rayleigh numbers. This interpretation would also be in line with the DNS results of the currently highest achievable Rayleigh numbers by Stevens *et al.* (2012). They found that agreement of a dynamically rescaled thermal boundary layer with the Pohlhausen prediction worsens when Ra grows.

One more point: the previous studies by Puthenveettil *et al.* (2011) as well as the recent experiments by Zhou & Xia (2010*a*) suggest that the velocity boundary layer is much less perturbed when the Prandtl number is increased. In this case, the thermal boundary layer thickness becomes much smaller than the thickness of

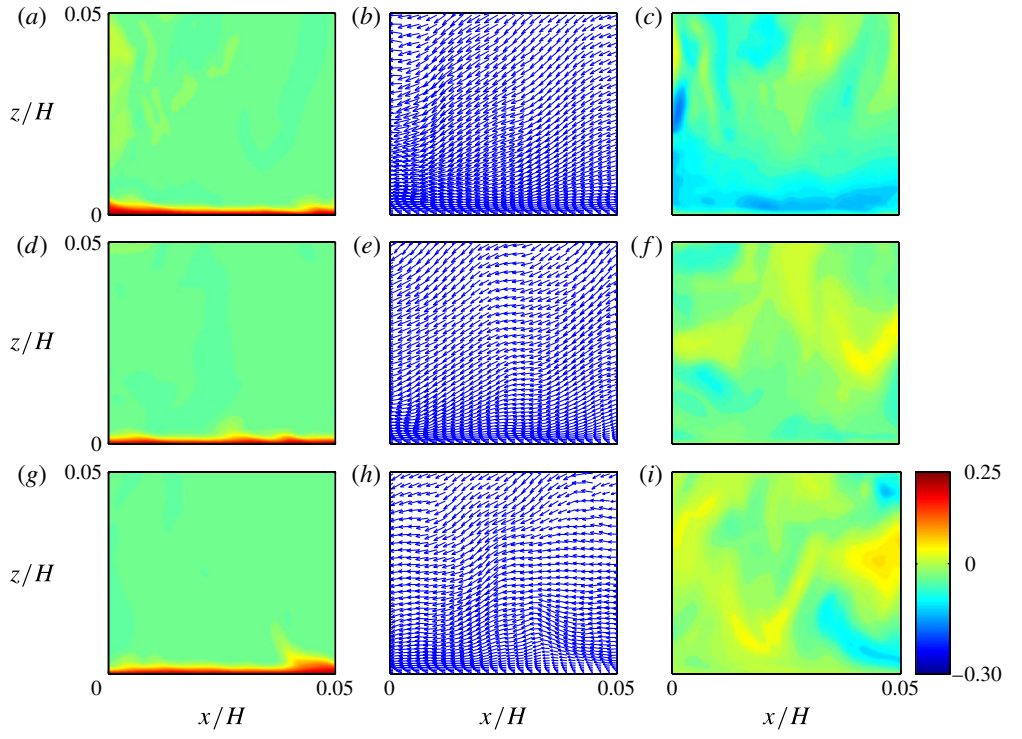

FIGURE 17. The same sequence of data as in figure 14 for $Ra = 3 \times 10^{10}$.

the velocity boundary layer. Plumes which detach will have a much narrower stem due to decreased thermal diffusion. We therefore expect that agreement with results from the laminar boundary layer theory will improve. This trend might, however, be compensated by an increasing number of fine-scale textures of the turbulent fields for increasing Rayleigh number. Our two streamline plots in figure 1 suggest this trend. Further comprehensive numerical and experimental studies are thus necessary to answer these questions.

Acknowledgements

The authors acknowledge support by the Deutsche Forschungsgemeinschaft (DFG) within the Research Group FOR1182, the Research Training Group GK1576 and the Heisenberg Programme under Grant No. SCHU 1410/5-1. The largest DNS simulations were carried out at the Jülich Supercomputing Centre (Germany) under Grant No. HIL02 on one rack of the Blue Gene/P JUGENE. J.S. was supported in part by the National Science Foundation under Grant No. PHY05-51164 within the programme 'The Nature of Turbulence', held at the Kavli Institute of Theoretical Physics at the University of California in Santa Barbara. We thank G. Ahlers, E. Bodenschatz, R. du Puits, D. Lohse, B. Puthenveettil, J. Scheel, A. Thess, P. Tong, R. Verzicco, S. Wagner and K.-Q. Xia for fruitful discussions. Special thanks to R. Verzicco for providing us with his original code and to J. R. Pacheco for an improved Poisson solver, which saved us a significant amount of CPU time.

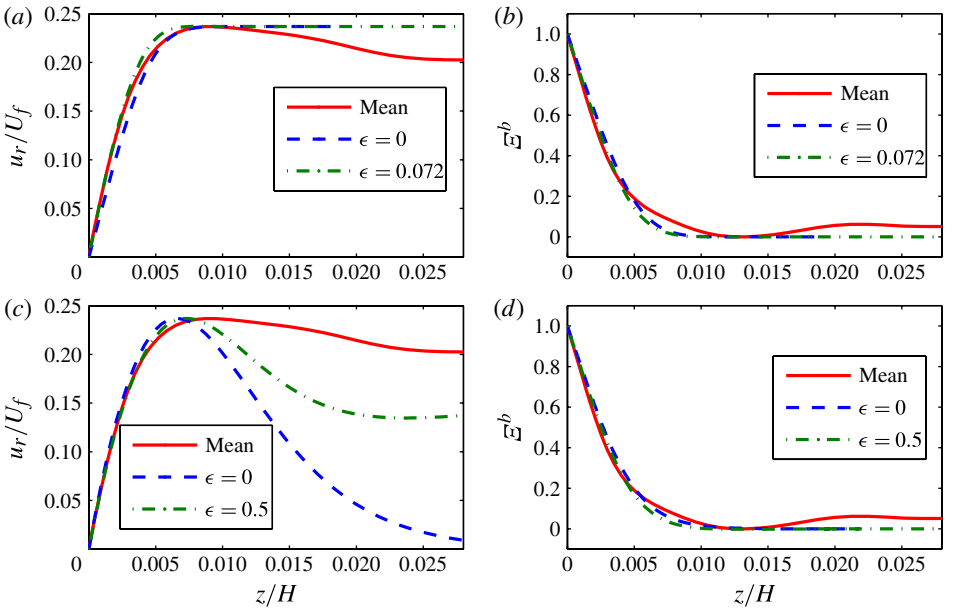

FIGURE 18. (Colour online) Matching of the time-averaged profiles of the plume detachment phase with the predictions from boundary layer analysis. The profiles are obtained as time averages from figure 13(*a*). Data are compared with purely forced and natural convection as well as with corresponding first-order perturbative expansions. (*a*) Radial velocity in units of U_f for forced convection. (*b*) Rescaled temperature for forced convection. (*c*) Radial velocity in units of U_f for natural convection. (*d*) Rescaled temperature for natural convection. Data are the same as in figures 12 and 13(*a*).

Appendix. Perturbative expansion of the boundary layer equations

We briefly review here the results reported in Stewartson (1958), Sparrow & Minkowycz (1962) and Hieber (1973). The similarity variable is given by

$$\eta = \begin{cases} z Re_x^{1/2}/x & \text{for forced convection,} \\ z Gr_x^{1/5}/x & \text{for natural convection,} \end{cases} \tag{A 1}$$

and the expansion parameter is given by

$$\epsilon = \begin{cases} Gr_x/Re_x^{5/2} & \text{for forced convection,} \\ Re_x/Gr_x^{2/5} & \text{for natural convection.} \end{cases} \tag{A 2}$$

Since the problem at hand is two-dimensional, one uses the stream function instead of the velocity components, which automatically satisfies the incompressibility condition (4.3). In the *forced* convection case the following expansions are taken,

$$\psi(x,z) = \sqrt{\nu x V_\infty}\left[\sum_{m=0}^{\infty} \epsilon^m f_m(\eta)\right], \tag{A 3}$$

$$T(x,z) = T_\infty + (T_w - T_\infty)\left[\sum_{m=0}^{\infty} \epsilon^m \theta_m(\eta)\right], \tag{A 4}$$

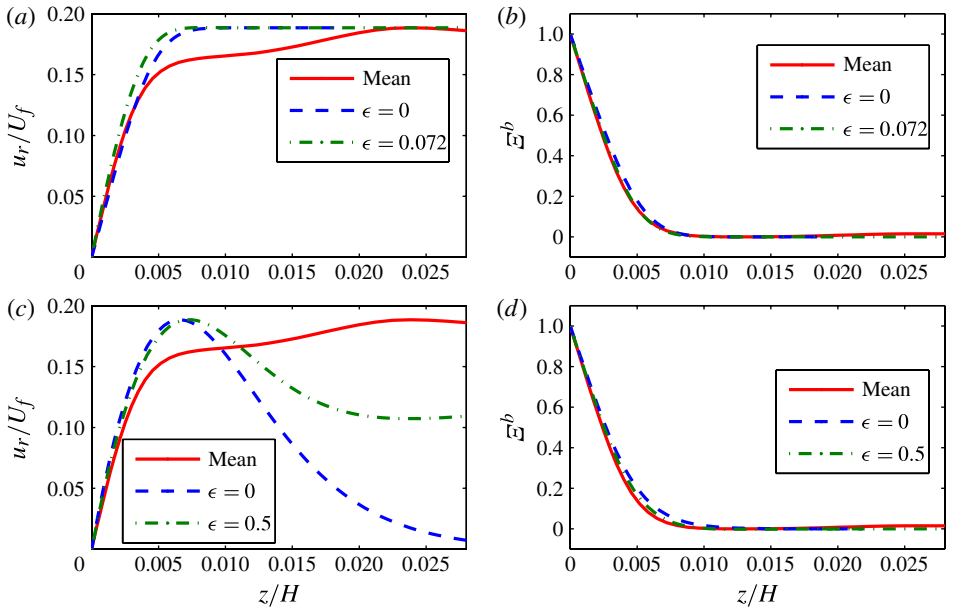

FIGURE 19. (Colour online) Matching of the time-averaged profiles of the post-plume-detachment phase with the predictions from boundary layer analysis. The profiles are obtained as time averages from figure 13(*b*). Panels (*a*)–(*d*) are as in figure 18. Data correspond to figures 13(*b*) and 14.

resulting for example in the following expressions for the velocity components,

$$u_x(x,z) = V_\infty \left[\sum_{m=0}^{\infty} \epsilon^m f_m'(\eta)\right], \tag{A 5}$$

$$u_z(x,z) = \frac{V_\infty}{2\sqrt{Re_x}} \left[(\eta f_0'(\eta) - f_0(\eta)) + \sum_{m=1}^{\infty} \epsilon^m \left(\eta f_m'(\eta) + \left(\frac{m}{2} - 1\right) f_m(\eta)\right)\right], \tag{A 6}$$

where primes denote derivatives with respect to η. The expansion generates in order ϵ^0 the classical Prandtl–Blasius–Pohlhausen equations

$$f_0''' + \frac{1}{2} f_0'' f_0 = 0, \tag{A 7}$$

$$\theta_0'' + \frac{Pr}{2} f_0 \theta_0' = 0. \tag{A 8}$$

The boundary conditions are $f_0(0) = f_0'(0) = 0$, $\theta_0(0) = 1$ and $f_0'(\infty) = 1$, $\theta_0(\infty) = 0$. The order ϵ^1 then reads

$$f_1''' + f_0'' f_1 + \frac{1}{2} f_0 f_1'' - \frac{1}{2} f_0' f_1' - \frac{1}{2} h_0 + \frac{\eta}{2} h_0' = 0, \tag{A 9}$$

$$h_0' = \theta_0, \tag{A 10}$$

$$\theta_1'' + \frac{Pr}{2} f_0 \theta_1' - \frac{Pr}{2} f_0' \theta_1 + Pr\, \theta_0' f_1 = 0. \tag{A 11}$$

The additional boundary conditions are $f_1(0) = f_1'(0) = \theta_1(0) = 0$ and $f_1'(\infty) = \theta_1(\infty) = h_0(\infty) = 0$. The last two terms of (A 9) containing h_0 and h_0' as well as (A 10) arise from the pressure term. In *natural* convection, the expansions are adapted to

$$\psi(x,z) = \sqrt[5]{\nu^3 g\alpha(T_w - T_\infty)x^3}\left[\sum_{m=0}^{\infty}\epsilon^m g_m(\eta)\right], \tag{A 12}$$

$$T(x,z) = T_\infty + (T_w - T_\infty)\left[\sum_{m=0}^{\infty}\epsilon^m \chi_m(\eta)\right]. \tag{A 13}$$

The order ϵ^0 was first discussed by Stewartson (1958) and given by

$$g_0''' + \frac{3}{5}g_0''g_0 - \frac{1}{5}g_0'g_0' - \frac{2}{5}k_0 + \frac{2}{5}\eta k_0' = 0, \tag{A 14}$$

$$k_0' = \chi_0, \tag{A 15}$$

$$\chi_0'' + \frac{3Pr}{5}g_0\chi_0' = 0. \tag{A 16}$$

The boundary conditions are $g_0(0) = g_0'(0) = 0$, $\chi_0(0) = 1$ and $g_0'(\infty) = \chi_0(\infty) = k_0(\infty) = 0$. The perturbative expansion to mixed convection with order ϵ^1 reads

$$g_1''' + \frac{3}{5}g_1''g_0 - \frac{1}{5}g_1'g_0' + \frac{2}{5}g_0''g_1 - \frac{1}{5}k_1 + \frac{2}{5}\eta k_1' = 0, \tag{A 17}$$

$$k_1' = \chi_1, \tag{A 18}$$

$$\chi_1'' + \frac{3Pr}{5}g_0\chi_1' + \frac{Pr}{5}g_0'\chi_1 + \frac{2Pr}{5}\chi_0'g_1 = 0, \tag{A 19}$$

with $g_1(0) = g_1'(0) = \chi_1(0) = \chi_1(\infty) = k_1(\infty) = 0$ and $g_1'(\infty) = 1$. Again, k_0 and k_1 arise from the pressure term. Equations (A 7)–(A 11) and (A 14)–(A 19) were solved in order to obtain the results displayed in figure 11.

REFERENCES

AHLERS, G., BODENSCHATZ, E., FUNFSCHILLING, D. & HOGG, J. 2009*a* Turbulent Rayleigh–Bénard convection for a Prandtl number of 0.67. *J. Fluid Mech.* **641**, 157–167.

AHLERS, G., GROSSMANN, S. & LOHSE, D. 2009*b* Heat transfer & large-scale dynamics in turbulent Rayleigh–Bénard convection. *Rev. Mod. Phys.* **81**, 503–537.

BAILON-CUBA, J., EMRAN, M. S. & SCHUMACHER, J. 2010 Aspect ratio dependence of heat transfer and large-scale flow in turbulent convection. *J. Fluid Mech.* **655**, 152–173.

BAILON-CUBA, J. & SCHUMACHER, J. 2011 Low-dimensional model of turbulent Rayleigh–Bénard convection in a Cartesian cell with square domain. *Phys. Fluids* **23**, 077101.

BLASIUS, H. 1908 Grenzschichten in Flüssigkeiten mit kleiner Reibung. *Z. Math. Phys.* **56**, 1–37.

BROWN, E. & AHLERS, G. 2009 The origin of oscillations of the large-scale circulation of turbulent Rayleigh–Bénard convection. *J. Fluid Mech.* **638**, 383–400.

EMRAN, M. S. & SCHUMACHER, J. 2008 Fine-scale statistics of temperature and its derivatives in convective turbulence. *J. Fluid Mech.* **611**, 13–34.

EMRAN, M. S. & SCHUMACHER, J. 2010 Lagrangian tracer dynamics in a closed cylindrical turbulent convection cell. *Phys. Rev.* E **82**, 016303.

FUJI, T. 1963 Theory of the steady laminar natural convection above a horizontal line source and a point heat source. *Intl J. Heat Mass Transfer* **6**, 597–606.

FUNFSCHILLING, D. & AHLERS, G. 2004 Plume motion and large-scale circulation in a cylindrical Rayleigh–Bénard cell. *Phys. Rev. Lett.* **92**, 194502.

GROSSMANN, S. & LOHSE, D. 2000 Scaling in thermal convection: a unifying theory. *J. Fluid Mech.* **407**, 27–56.

GRÖTZBACH, G. 1983 Spatial resolution requirements for direct numerical simulation of the Rayleigh–Bénard convection. *J. Comput. Phys.* **49**, 241–264.

HIEBER, C. A. 1973 Mixed convection above a heated horizontal surface. *Intl J. Heat Mass Transfer* **16**, 769–785.

MISHRA, P. K., DE, A. K., VERMA, M. K. & ESWARAN, V. 2011 Dynamics of reorientations and reversals of large-scale flow in Rayleigh–Bénard convection. *J. Fluid Mech.* **668**, 480–499.

POHLHAUSEN, E. 1921 Der Wärmetausch zwischen festen Körpern und Flüssigkeiten mit kleiner Reibung und kleiner Wärmeleitung. *Z. Angew. Math. Mech.* **1**, 115–121.

PRANDTL, L. 1905 Über Flüssigkeitsbewegung bei sehr kleiner Reibung. In *Proceedings of the Third International Mathematicians' Congress, Heidelberg, 1904*, pp. 484–491. B. G. Teubner.

DU PUITS, R., RESAGK, C. & THESS, A. 2007*a* Mean velocity profile in confined turbulent convection. *Phys. Rev. Lett.* **99**, 234504.

DU PUITS, R., RESAGK, C. & THESS, A. 2007*b* Breakdown of wind in turbulent thermal convection. *Phys. Rev.* E **75**, 016302.

DU PUITS, R., RESAGK, C. & THESS, A. 2010 Measurements of the instantaneous local heat flux in turbulent Rayeigh–Bénard convection. *New J. Phys.* **12**, 075023.

PUTHENVEETTIL, B. A. & ARAKERI, J. H. 2005 Plume structure in high-Rayleigh-number convection. *J. Fluid Mech.* **542**, 217–249.

PUTHENVEETTIL, B. A., GUNASEGARANE, G. S., AGRAWAL, Y. K., SCHMELING, D., BOSBACH, J. & ARAKERI, J. H. 2011 Length of near-wall plumes in turbulent convection. *J. Fluid Mech.* **685**, 335–364.

ROTEM, Z. & CLAASSEN, L. 1969 Natural convection above unconfined horizontal surfaces. *J. Fluid Mech.* **39**, 173–192.

SCHLICHTING, H. 1957 *Boundary Layer Theory*. McGraw-Hill.

SHISHKINA, O., STEVENS, R. J. A. M., GROSSMANN, S. & LOHSE, D. 2010 Boundary layer structure in turbulent thermal convection and its consequences for the required numerical resolution. *New J. Phys.* **12**, 075022.

SHISHKINA, O. & WAGNER, C. 2008 Analysis of sheet-like thermal plumes in turbulent Rayleigh–Bénard convection. *J. Fluid Mech.* **599**, 383–404.

SIGGIA, E. D. 1994 High Rayleigh number convection. *Annu. Rev. Fluid Mech.* **26**, 137–168.

SPARROW, E. M. & MINKOWYCZ, W. J. 1962 Buoyancy effects on horizontal boundary-layer flow and heat transfer. *Intl J. Heat Mass Transfer* **5**, 505–511.

STEVENS, R. J. A. M., ZHOU, Q., GROSSMANN, S., VERZICCO, R., XIA, K.-Q. & LOHSE, D. 2012 Thermal boundary layer profiles in turbulent Rayleigh–Bénard convection in a cylindrical sample. *Phys. Rev.* E **85**, 027301.

STEWARTSON, K. 1958 On the free convection from a horizontal plate. *Z. Angew. Math. Phys.* **9**, 276–282.

SUN, C., CHEUNG, Y.-H. & XIA, K.-Q. 2008 Experimental studies of the viscous boundary layer properties in turbulent Rayleigh–Bénard convection. *J. Fluid Mech.* **605**, 79–113.

THEERTHAN, S. A. & ARAKERI, J. H. 1998 A model for near-wall dynamics in turbulent Rayleigh–Bénard convection. *J. Fluid Mech.* **373**, 221–254.

VAN REEUWIJK, M., JONKER, H. J. J. & HANJALIĆ, K. 2008*a* Wind and boundary layers in Rayleigh–Bénard convection. Part 1. Analysis and modelling. *Phys. Rev.* E **77**, 036311.

VAN REEUWIJK, M., JONKER, H. J. J. & HANJALIĆ, K. 2008*b* Wind and boundary layers in Rayleigh–Bénard convection. Part 2. Boundary layer character and scaling. *Phys. Rev.* E **77**, 036312.

VERZICCO, R. & CAMUSSI, R. 2003 Numerical experiments on strongly turbulent thermal convection in a slender cylindrical cell. *J. Fluid Mech.* **477**, 19–49.

VERZICCO, R. & ORLANDI, P. 1996 A finite-difference scheme for three-dimensional incompressible flows in cylindrical coordinates. *J. Comput. Phys.* **123**, 402–414.

XI, H.-D. & XIA, K.-Q. 2008*a* Azimuthal motion, reorientation, cessation, and reversal of the large-scale circulation in turbulent thermal convection: a comparative study in aspect ratio one and one-half geometries. *Phys. Rev.* E **78**, 036326.

XI, H.-D. & XIA, K.-Q. 2008*b* Flow mode transitions in turbulent thermal convection. *Phys. Fluids* **20**, 055104.

ZHOU, Q., STEVENS, R. J. A. M., SUGIYAMA, K., GROSSMANN, S., LOHSE, D. & XIA, K.-Q. 2010 Prandtl–Blasius temperature and velocity boundary-layer profiles in turbulent Rayleigh–Bénard convection. *J. Fluid Mech.* **664**, 297–312.

ZHOU, Q., SUGIYAMA, K., STEVENS, R. J. A. M., GROSSMANN, S., LOHSE, D. & XIA, K.-Q. 2011 Horizontal structures of velocity and temperature boundary layers in two-dimensional numerical turbulent Rayleigh–Bénard convection. *Phys. Fluids* **23**, 125104.

ZHOU, Q., SUN, C. & XIA, K.-Q. 2007 Morphological evolution of thermal plumes in turbulent Rayleigh–Bénard convection. *Phys. Rev. Lett.* **98**, 074501.

ZHOU, Q. & XIA, K.-Q. 2010*a* Measured instantaneous viscous boundary layer in turbulent Rayleigh–Bénard convection. *Phys. Rev. Lett.* **104**, 104301.

ZHOU, Q. & XIA, K.-Q. 2010*b* Physical and geometrical properties of thermal plumes in turbulent Rayleigh–Bénard convection. *New J. Phys.* **12**, 075006.